

Dependence of Wear and Corrosion Properties on the Electron Work Function

by

Xiaochen Huang

A thesis submitted in partial fulfillment of the requirements for the degree of

Master of Science

in

Materials Engineering

Department of Chemical and Materials Engineering
University of Alberta

© Xiaochen Huang, 2015

Abstract

Mechanical, tribological and corrosion properties of metallic materials are of significance to their industrial applications and have been studied for long time. Efforts are continuously made to correlate these properties to more fundamental parameters in order to effectively improve the materials. Electron work function (EWF) is a fundamental property of metals which characterizes their electron behavior and can be experimentally obtained with ease. This simple but fundamental parameter reflects the difficulty of changing the electronic state, which can be related to material's performance in wear and corrosion.

In this study, attempts were made to establish relationships among EWF, mechanical and tribological properties and corrosion behaviors. The dependence of metallic material's wear resistance was also investigated via EWF. Higher EWF corresponds to higher Young's modulus and hardness, more stable electronic state, and thus the better performance in solid-particle erosion, slurry erosion and acid-medium corrosion tests. In sliding wear and neutral-medium corrosion tests, this correlation between EWF and material's performance was concealed due to the influence of oxidation. Using the relationship between EWF and temperature, further erosion tests at elevated temperature made it possible to predict metallic material's wear resistance via EWF.

Acknowledgements

I especially want to thank my supervisor, Professor Dongyang Li. His kind suggestions, patient guidance, and insightful criticisms benefited me in both detailed experiment deployments and summarizing the whole work from an in-depth viewpoint, including the writing of this thesis.

I would like to thank the professors who were in my committee and made helpful comments on my thesis.

My special thanks are due to my group members from whom I obtained useful suggestions and experience.

I would also like to say thank you to my parents who always support me and keep encouraging me.

Financial support provided to this project by the Natural Science and Engineering Research Council of Canada (NSERC) and AUTO21 is gratefully acknowledged.

Table of Contents

Chapter 1 Introduction and Literature Review	1
1.1 General Introduction to the electron work function (EWF).....	2
1.1.1 Definition	2
1.1.2 Measurements.....	3
1.1.3 Theoretical Analysis	5
1.1.4 Correlation with other properties	7
1.1.4.1 Electron work function and atomic number	7
1.1.4.2 Electron work function and interface barrier	8
1.1.4.3 Electron work function and surface energy.....	8
1.1.4.4 Electron work function and adhesion force	9
1.1.4.5 Electron work function and Young’s modulus.....	11
1.1.4.6 Electron work function and yield strength	13
1.1.4.7 Electron work function and hardness.....	14
1.1.4.8 Electron work function and number of transferred electrons	14
1.1.4.9 Electron work function and electrode potential	15
1.2 General introduction to the Cu-Ni binary system	16
1.3 Correlation between the wear resistance of Cu-Ni alloy and its EWF.....	18
1.4 Correlation between the corrosion and corrosive wear resistance of Cu-Ni alloys and its EWF.....	19
1.5 Dependence of erosive wear on temperature via the electron work function..	22
Chapter 2 Correlation between the wear resistance of isomorphous Cu-Ni alloy and its electron work function.....	26
2.1 Objectives	27
2.2 Experimental procedures	27
2.3 Results and discussion.....	30
2.3.1 EWF measurement	30
2.3.2 Correlation between EWF and Young’s modulus and Hardness.....	32
2.3.3 Resistance to sliding wear and its relation with EWF.....	33
2.3.4 Resistance to solid particle erosion and its relation with EWF	38
2.4 Summary	44
Chapter 3 Correlation between corrosion resistance and corrosive wear and EWF	46
3.1 Objectives	47
3.2 Experimental procedures	47

3.3 Results and discussions	49
3.3.1 Corrosion behavior	49
3.3.2 Corrosive wear	59
3.4 Summary	65
Chapter 4 Dependence of metallic material’s wear resistance on temperature via the electron work function	66
4.1 Objectives	67
4.2 Experimental procedures	67
4.3 Results and discussion.....	67
4.2 Summary	73
Chapter 5 General conclusions and future work.....	75
5.1 General conclusions of the research	76
5.2 Future work	77
5.2.1 Influence of second phases on the mechanical/corrosion property-EWF correlation	77
5.2.2 More fundamental studies on the relationship between EWF and the electrode potential	78
5.2.3 Using improved models and experiment techniques	78
Reference	79

List of Tables

Table 1.1 The periodic table of elements.	8
Table 1.2 EWF and adhesion force of single crystal copper with different crystallographic planes[32].	10
Table 2.1 Compositions of the Cu-Ni alloys made for the study.	28
Table 2.2 Spot Energy Dispersive Spectroscopy (EDS) analysis of Cu, Ni and 50Cu-50Ni after sliding wear.	36
Table 2.3 Spot EDS analysis of Samples Cu, Ni and 50Cu-50Ni after erosion.....	41
Table 3.1 Spot Energy Dispersive Spectroscopy (EDS) analysis of the samples after immersion in NaCl and in HCl.	54
Table 3.2 Weight losses of Cu and Ni when respectively immersed in NaCl and HCl solutions in two arrangements: separated and connected.....	58
Table 3.3 Spot Energy Dispersive Spectroscopy (EDS) analysis of the samples after corrosive wear in NaCl and in HCl.....	62
Table 3.4 EDS analysis of eroded surfaces of three samples.....	64
Table 4.1 Values of the coefficient γ and β of the materials under different conditions.	71

List of Figures

Figure 1.1 The illustration of EWF, electron energy and potential well.....	2
Figure 1.2 Some applications of Cu-Ni alloys.....	17
Figure 2.1. SEM backscattered images of samples (a) 80Cu-20Ni, (b) 50Cu-50Ni and (c) 10Cu-90Ni.....	28
Figure 2.2 Electron work functions of the fabricated alloys measured with UPS.	31
Figure 2.3 Young's modulus (a) and hardness (b) of the fabricated Cu-Ni alloys.	33
Figure 2.4 Sliding wear loss of Cu-Ni samples with different concentrations of Ni.	35
Figure 2.5 SEM images of worn surface of three selected alloys. (a) Cu, (b) Ni, and (c) 50Cu-50Ni.....	36
Figure 2.6 Erosion rates of the fabricated alloys with three impingement angles.	40
Figure 2.7 Eroded surfaces of three samples after erosion under the 90° air-jet solid particle erosion condition: (a) Cu; (b) Ni and (c) 50Cu-50Ni.....	41
Figure 2.8 Erosion loss against the work function.	44
Figure 3.1 Surface roughness of samples after immersion in NaCl solution for 7 days. (a) Cu, (b) 80Cu-20Ni, (c) 50Cu-50Ni, (d) 20Cu-80Ni and (e) Ni.....	50
Figure 3.2 Surface roughness of samples after immersion in HCl solution for 7 days. (a) Cu, (b) 80Cu-20Ni, (c) 50Cu-50Ni, (d) 20Cu-80Ni and (e) Ni.....	51
Figure 3.3 SEM images of the surfaces after immersion in NaCl. (a) Cu, (b) 80Cu-20Ni, (c) 50Cu-50Ni, (d) 20Cu-80Ni and (e) Ni.	52
Figure 3.4 SEM images of the surfaces after immersion in HCl. (a) Cu, (b) 80Cu-20Ni, (c) 50Cu-50Ni, (d) 20Cu-80Ni and (e) Ni.	53
Figure 3.5 Corrosive wear loss of the alloys in two solutions: (1) 3 wt.% NaCl and (2) HCl with a pH=3.....	60
Figure 3.6 SEM images of worn surfaces in NaCl solution of three selected samples: (a) Cu sample (#1), (b) Ni (#5), and (c)50Cu-50Ni (#3).....	61
Figure 3.7 SEM images of worn surfaces in HCl of three selected alloys. (a) Cu, (b) Ni, and (c) 50Cu-50Ni.	61
Figure 3.8 Material loss caused by slurry-jet erosion. Slurry: sand-containing NaCl solution.	63
Figure 3.9 Eroded surfaces of (a) Cu, (b) Ni and (c) 50Cu-50Ni.	64

Figure 4.1 Variations in mass loss of copper, nickel and steel samples with temperature and sand particle velocity. The curves present the theoretical prediction and the data points are from the experimental measurements..... 70

Figure 4.2 SEM images of the eroded surfaces of copper, nickel and carbon steel under room temperature, 100°C and 300°C, respectively..... 73

List of Symbols

a	Lattice constant
A_c	Contact area
b	Burgers vector
d	Initial distance between the electron and surface
e	Elementary charge
E_f	Fermi energy
E_K	Kinetic energy of an emitted photoelectron
E^M	Electrode potential
$E_T(ref)$	Potential barrier at the reference electrode
F	Normal load applied to the worn surface
$g^{S^*}(dip)$	Contribution due to preferentially orientated solvent molecules
$g_{S^*}^M(ion)$	Additional potential drop due to the presence of free charges
h	Planck's constant
H	Hardness
H_{vap}	Molar heat of vaporization
I	Ionization energy for the formation of singly charged ion
k_B	Boltzmann constant
K_W	Wear coefficient
l	Sliding distance
m	Mass of electron
\bar{m}	Applied stress orientation
n_{ws}	Wigner-Seitz electron density parameter
r	Instantaneous distance between the electron and surface
r_e	Equilibrium distance between two atoms
ν	Frequency of the ionization light
v_y	Vertical component of the velocity

V_M	Molar volume
$V(r)$	Lennard-Jones potential
w_i	An energy contribution factor
WL	Material volume loss during wear process
α	Madelung constant
α_L	Linear thermal expansion coefficient
γ	Material's structure constant
ρ	Density of material
μ	Shear modulus
ν	Poisson ratio
ξ	Width of a dislocation
σ_y	Yielding strength
φ	Electron work function
γ_s	Surface energy
ϵ_0	Vacuum permittivity
ϵ_b	Maximum value for the depth of the potential well
ΔN	Number of transferred electrons
$\Delta\varphi$	Difference of electron work function
$\Delta_s^m\psi$	Contact potential difference at the metal/solution interface
$\sum E_g^{AV}$	Average energy gap
$\delta\chi_\sigma^M$	Modification factor

List of Abbreviations

AFM	Atomic Force Microscope
ASTM	American Society for Testing and Materials
CPD	Contact Potential Difference
EDS	Energy Dispersive Spectroscopy
EFW	Electron Work Function
SEM	Scanning Electron Microscope
UPS	Ultraviolet Photoelectron Spectroscopy

Chapter 1

Introduction and Literature Review

1.1 General Introduction to the electron work function (EWF)

1.1.1 Definition

The electron work function (EWF) is defined as the threshold energy required to extract electrons at the Fermi level from the inside of a metal to its surface without kinetic energy [1]. Figure 1.1 demonstrates the physical meanings of electron work function, electron energy and potential well in a visual way. Or alternatively, EWF is the energy for moving electrons at Fermi level inside a metal to a point far enough outside its surface so that the image force can be neglected. EWF depends on the composition of material and the density of valence electrons as well as the charge redistribution caused by a dipole layer formed at the material surface [2].

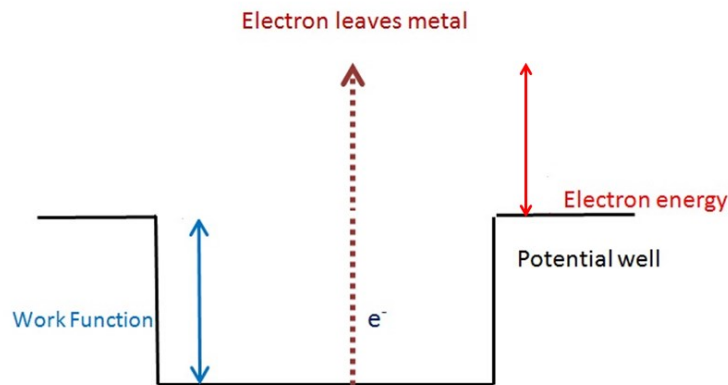


Figure 1.1 The illustration of EWF, electron energy and potential well

As a fundamental electronic property of a metallic surface, EWF largely reflects the electron behavior and is thus a sensitive indicator of surface condition, such as adsorption [3], surface roughness and corrosion products [4], and catalysis [5], etc., providing invaluable information to understand surface and interface physics

and chemistry [6], which is crucial for development of advanced materials. For instance, the work function dominates the oriented mobility of positive and negative charges, which is an important function of heterogeneous junctions in microelectronics [7], photocatalysis [8], sensor technology [9], solar cells [10], etc. Although strongly influenced by the surface condition, the electron work function is a fundamental parameter reflecting intrinsic properties of bulk materials [11, 12]. If the atomic interaction can be related correlated to EWF in a straightforward way, in-depth understanding of intrinsic mechanical and corrosion properties on an electronic base could be readily achieved. This could also provide an alternative approach and complementary clues for advanced materials design. However, studies in this area are limited.

1.1.2 Measurements

The measurements of the electron work function can be divided into direct and indirect techniques. Direct techniques are based on the emission of electrons from a surface. These techniques, depending on the external excitations, can be subdivided into thermoemission, photoemission and exoelectronic emission. Ultraviolet Photoelectron Spectroscopy (UPS), for instance, is used to measure EWF based on Einstein's photoelectric law:

$$E_K = h\nu - I \quad (1.1)$$

where E_K is the kinetic energy of an emitted photoelectron, h is Planck's constant, ν is the frequency of the ionization light, and I is an ionization energy for the formation of singly charged ion in either the ground state or an excited state.

The full width of the photoelectron spectrum can be defined as the cutoff from the highest kinetic energy/lowest binding energy point to the lowest kinetic energy, which is measured and subtracted from the photon energy of the exciting radiation, and the difference is the work function. Often, the sample is electrically biased negative to separate the low energy cutoff from the spectrometer response [13].

Indirect techniques includes the methods that study the effects of its surface on an external beam of electrons, as well as that measure the contact potential difference (CPD) between its own surface and a reference surface [14-16].

CPD between two surfaces is known as the potential difference between them when they are brought together (electrical contact) and when thermodynamic equilibrium is achieved. Two typical CPD measurement techniques are ionization and capacitor techniques. The application of ionization technique is limited, since it requires a radioactive source. What people use most frequently nowadays is the Kelvin method. Kelvin method is based on CPD and has drawn increasing interest and has been widely applied in the investigation of various material behaviors [11, 15, 17-19]. A surface potential barrier is formed to restrict the free electrons within a metal from escaping. When the two plates are connected electrically, thermodynamic

equilibrium is achieved when the Fermi energy levels for the two metal plates are equal. Electrons just outside the metal surfaces have different potentials since the equality of the Fermi levels is obtained by the flow of electrons from the plate with the lower work function to that with the higher one. The first metal surface is charged positively and the second is charged negatively. The contact potential difference U_{CPD} , is defined here as the difference between the electron work functions of the two metals divided by the charge of one electron. [6, 14]:

$$U_{CPD} = (\varphi_2 - \varphi_1)/e \quad (1.2)$$

The Kelvin probe is a noncontact and nondestructive vibrating capacitor device used to measure the work function difference between a conducting specimen and a vibrating tip. It has been widely applied under various conditions including ambient, vacuum and even fluid environment [14, 16].

1.1.3 Theoretical Analysis

The evaluations of the work functions of the elements have drawn great interest from scientists all over the world for over one century. Taking density, electronic valence as well as atomic weight into consideration, Rother and Bomke put forward an empirical expression for φ . Chittum and Gombas correlated the electron work function with the lattice energy in the crystal, Bartclink found an approximate relationship between EWF and the reciprocal of atomic volume for the alkali metals,

Wigner and Bardeen developed another equation for work functions of the univalent metals in terms of the sublimation heat [20].

Other methods such as Jellium calculations were also developed to calculate electron work function. Self-consistent Green's-function technique based on Andersen's tight-binding linear muffin-tin-orbital (TB-LMTO) method was also used in EWF calculation [20-22]. In 1995, based on the electrostatic image potential energy, Brodie calculated EWF without taking ab initio methods. According to his model, the work function of polycrystalline metallic surface is related to the atomic radius, Fermi energy, and effective mass of an electron. Brodie's simple model produced results in very good agreement with experimental data. This approach was later further improved by Halas and Durakiewicz, who applied the so-called metallic plasma model [1, 23, 24].

To investigate the influence of a dislocation on EWF, D.Y. Li and W. Li proposed a model which takes the electrostatic action between electron and nuclei into consideration [25]. Theoretical analysis by the authors pointed out that the deviation of EWF depends on the type of deformation: EWF decreases when subjected to elastic tension while increases under elastic compression. However, when plastic deformation occurs, the EWF always decreases as a result of the formation of dislocations.

1.1.4 Correlation with other properties

EFW can be related with many other properties of materials since EWF is such a fundamental electronic property of metallic solids characterizing the electronic stability. It has been known for a long time that EWF correlates well with many atomic properties such as ionization energies, electron affinity and electronegativity [26, 27]. It was reported that EWF is approximately half the value of the ionization energy [1]. EWF also correlates with $n_{ws}^{1/3}$, $(H_{vap}/V_M^{2/3})^{1/3}$ and $V_M^{-1/3}$, where n_{ws} is the Wigner-Seitz electron density parameter, H_{vap} is the molar heat of vaporization, and V_M is the molar volume [26].

1.1.4.1 Electron work function and atomic number

The relationship between the electron work function and atomic number has been widely recognized and reported in the literature. Selecting and analyzing the experimental results published during the period from 1924-1949, Michaelson plotted the work function, first ionization potential, and standard electrode potential of 57 elements versus atomic number. The result shows a good periodicity of the work function, like many other chemical properties [20]. The currently accepted experimental data of EWF is summarized and shown in Table 1.1 [1]. In the table, under the symbols of elements, the upper row numbers are ionization energies, the middle row numbers are EWFs and the lower row numbers are electron affinities, given in eV/atom.

Table 1.1 The periodic table of elements.

¹ H 13.598 0.7542																	² He 24.58 -0.22
³ Li 5.39 2.9 0.6182	⁴ Be 9.32 4.98 -0.19											⁵ B 8.30 4.45 0.227	⁶ C 11.26 5.0 1.2629	⁷ N 14.54 -0.07	⁸ O 13.61 1.462	⁹ F 17.42 3.399	¹⁰ Ne 21.56 -0.3
¹¹ Na 5.14 2.75 0.5479	¹² Mg 7.64 3.66 -0.22											¹³ Al 5.98 4.28 0.442	¹⁴ Si 8.15 4.85 1.385	¹⁵ P 10.55 2.077	¹⁶ S 10.36 3.615	¹⁷ Cl 13.01 2.0208	¹⁸ Ar 15.76 -0.36
¹⁹ K 4.34 2.30 0.5015	²⁰ Ca 6.11 2.87 0.0215	²¹ Sc 6.56 3.4 0.189	²² Ti 6.83 4.33 0.080	²³ V 6.74 4.3 0.526	²⁴ Cr 6.76 4.5 0.667	²⁵ Mn 7.43 4.1 <0.005	²⁶ Fe 7.90 4.5 0.164	²⁷ Co 7.86 5.0 0.662	²⁸ Ni 7.63 5.15 1.157	²⁹ Cu 7.72 4.51 1.228	³⁰ Zn 9.39 4.33 0.093	³¹ Ga 6.00 4.15 0.31	³² Ge 7.89 5.0 1.23	³³ As 9.81 4.77 0.81	³⁴ Se 9.75 5.9	³⁵ Br 11.84 3.364	³⁶ Kr 14.00 <0
³⁷ Rb 4.18 2.16 0.4859	³⁸ Sr 5.69 2.59 0.11	³⁹ Y 6.38 3.1 0.308	⁴⁰ Zr 6.95 4.05 0.427	⁴¹ Nb 6.88 4.3 0.894	⁴² Mo 7.18 4.6 0.747	⁴³ Tc 7.28 4.9 0.55	⁴⁴ Ru 7.36 4.71 1.05	⁴⁵ Rh 7.46 4.98 1.138	⁴⁶ Pd 8.343 5.12 0.558	⁴⁷ Ag 7.57 4.26 1.303	⁴⁸ Cd 8.99 4.22 0.260	⁴⁹ In 5.78 4.12 0.30	⁵⁰ Sn 7.34 4.42 1.15	⁵¹ Sb 8.64 4.55 1.07	⁵² Te 9.01 4.95 1.9708	⁵³ I 10.45 3.059	⁵⁴ Xe 12.13 <0
⁵⁵ Cs 3.893 2.14 0.4716	⁵⁶ Ba 5.21 2.7 0.17	⁵⁷ La 5.57 3.1 0.518	⁷² Hf 7.00 3.9 ≥0.1	⁷³ Ta 7.89 4.25 0.323	⁷⁴ W 7.98 4.55 0.816	⁷⁵ Re 7.87 4.87 0.12	⁷⁶ Os 8.70 4.83 1.12	⁷⁷ Ir 9.0 5.27 1.566	⁷⁸ Pt 8.96 5.65 2.128	⁷⁹ Au 9.22 5.1 2.309	⁸⁰ Hg 10.43 4.49 0.186	⁸¹ Tl 6.11 3.84 0.3	⁸² Pb 7.41 4.25 0.364	⁸³ Bi 7.29 4.22 0.946	⁸⁴ Po 8.43 5.0	⁸⁵ At 9.64 2.8	⁸⁶ Rn 10.74 <0
⁸⁷ Fr 3.98 2.1	⁸⁸ Ra 5.28 2.8 0.17	⁸⁹ Ac 5.17 3.2	⁵⁸ Ce 5.466 2.97 0.518	⁵⁹ Pr 5.42 2.96 ≥0.1	⁶⁰ Nd 5.49 3.2 ≥0.05	⁶¹ Pm 5.54 3.1	⁶² Sm 5.6 2.85 ≥0.05	⁶³ Eu 5.67 2.5 ≥0.05	⁶⁴ Gd 6.14 3.17 ≥0.1	⁶⁵ Tb 5.85 3.15 ≥0.1	⁶⁶ Dy 5.93 3.25 0.15	⁶⁷ Ho 6.02 3.22 <0.005	⁶⁸ Er 6.10 3.25 <0.005	⁶⁹ Tm 6.18 3.1 0.035	⁹⁰ Yb 6.25 3.0	⁹¹ Lu 6.25 3.0	⁹² Hf 6.25 3.0
⁹⁰ Th 6.08 3.4 >0.05	⁹¹ Pa 5.89 3.7 >0.05	⁹² U 6.05 3.63 >0.05	⁹³ Np 6.19 3.9	⁹⁴ Pu 6.06 3.6 ≥0.05	⁹⁵ Am 6.00 3.7	⁹⁶ Cm 6.02 3.9	⁹⁷ Bk 6.23 3.8	⁹⁸ Cf 6.30 4.0	⁹⁹ Bk 6.42 3.3	¹⁰⁰ Fm	¹⁰¹ Md	¹⁰² No					

1.1.4.2 Electron work function and interface barrier

Ferrante showed that EWF can be reflected by the bimetallic interface barrier. For same metal interface, the barrier approaches the EWF of the metal; while for two different metals, the barrier is intermediate between EWFs of the two metals.

1.1.4.3 Electron work function and surface energy

During the formation process of a binary alloy, charge transfers from one constituent to the other to equalize the electrochemical potential throughout the

crystal. Thus EWF can be regarded as an important parameter in estimating the surface energy of alloys if the relationship between surface energy of an alloy and its heat of formation can be clarified. Using the data of surface energies of liquid metals, Miedema suggested a semi-empirical equation to relate the surface energy of a metal to its electronic properties as the following equation [28]:

$$\gamma_s = n_{ws}^{\frac{5}{3}} / (\varphi^* - 0.6)^2 \quad (1.3)$$

where γ_s is the surface energy of a metal at 0 K; n_{ws} is the electron density at the boundary of the Wigner-Seitz cell; φ^* is a parameter approximately equal to EWF of a metal and related to its electronegativity [27-30].

Kalazhokov et al. [31] further developed the relation between surface energy and EWF. Surface energy was expressed as a function of EWF as follows

$$\gamma_i = \left(2 - \frac{\varphi_i}{\varphi_0}\right) \varphi_0 \quad (1.4)$$

where φ_0 is the EWF of the polycrystalline surface.

1.1.4.4 Electron work function and adhesion force

It has been found that EWF can be related to crystallographic orientation and adhesion force [32]. Table 1.2 shows EWF and adhesion force (AF) of different crystallographic planes of copper. It shows that EWF decreased as the surface atomic packing density decreased in the following order (011), (112), (321) and (413). And

the relationship between AF and EWF can be generalized from the data: the lower the ϕ , the higher is the adhesion force. This trend indicates that EWF is a parameter reflecting the adhesive force.

Table 1.2 EWF and adhesion force of single crystal copper with different crystallographic planes[32].

Orientation	(011)	(321)	(112)	(413)
ϕ (eV)	4.59	4.12	4.56	4.00
F (nN)	17.3	19.4	17.4	21.3

Great agreement was achieved when such a trend of experimental data was compared with the theoretical analysis. An electrostatic force model indicates that if small disturbance from the formation of the electric double layer at surface can be neglected, the EWF is mainly dependent on the electrostatic interaction between electrons and nuclei in the surface layer. And this can explain why a closely packed plane has a higher EWF: an electron is subjected to higher attractive forces from positive nuclei [33].

Adhesive force is strongly dependent on the surface arrangement. According to a “broken bond model” for surface energy, a closely packed plane has a lower surface energy than a loosely packed plane, because a closely packed plane has few broken bonds that are active, which can lead to fewer positions to interact with

foreign atoms or the surface is less active when in contact with another surface, thus a lower adhesive force can be achieved [32].

Both the adhesive force and EWF have strong dependence on the arrangement and nature of atoms in the surface layer, so the EWF can be regarded as a parameter that reflects the adhesion characteristic of a surface. Studies have shown that, even for more complicated surface structures involving, e.g., adsorption of foreign atoms and lattice distortion due to residual stress, using an electrostatic force model [32, 33], the correlation between adhesion force and the electron work function can still be built.

1.1.4.5 Electron work function and Young's modulus

Young's modulus here is defined as the second-order derivative of interaction potential with respect to the equilibrium distance [34]. Based on the image charge method [35], Guomin [36] derived the expression for work function as follows:

$$\varphi = W_{image} = \int_d^{\infty} \frac{e^2}{4\pi\epsilon_0(2r)^2} dr = \frac{e^2}{16\pi\epsilon_0 d} \quad (1.5)$$

where d is the initial distance between the electron and surface, ϵ_0 is vacuum permittivity, and r is the instantaneous distance between the electron and surface during the process of moving the electron away from the surface. Combined with Halas and Durakiewicz's description of d [24]:

$$d = \sqrt{\frac{2\varepsilon_0 E_f}{ne^2}} \quad (1.6)$$

and the expression of Fermi energy, E_f with respect to electron density, n , the expression for electron work function in terms of electron density is obtained:

$$\varphi = \frac{e^3 m^{1/2} n^{1/6}}{16^3 \sqrt{3} \pi^{5/3} \hbar \varepsilon_0^{3/2}} \quad (1.7)$$

The correlation between EWF and Young's modulus is finally expressed as

$$E = 2\alpha z e^2 \left(\frac{16^3 \sqrt{3} \pi^{5/3} \hbar \varepsilon_0^{3/2}}{e^3 m^{1/2} z^{1/6}} \right)^6 \varphi^6 = \alpha \frac{18 \times 16^6 \pi^{10} \hbar^6 \varepsilon_0^9}{e^{16} m^3} \varphi^6 \propto \alpha \varphi^6 \quad (1.8)$$

in which α is the Madelung constant, e and m are the elementary charge and the mass of electron, respectively. \hbar is the reduced Planck constant. Though the relationship between Young's modulus and EWF should also be influenced by the differences in crystal structures, which can be reflected by the Madelung constant α , as well as the number of valence electrons, these influences are much smaller than the responding change in φ due to the sixth power as expresses in Eq.(1.8). Actually this theoretical $E - \varphi$ correlation is in good agreement with the experimental data [36].

1.1.4.6 Electron work function and yield strength

Though also influenced by other factors such as the activated slip systems, the yield strength is intrinsically dependent on the atomic bonding. According to the Peierls-Nabarro model [37, 38], the misfit energy of an edge dislocation is expressed as [39]

$$W_{(\mu)} = \frac{\mu b^2}{4\pi(1-\nu)} + \frac{\mu b^2}{2\pi(1-\nu)} \exp\left(-\frac{4\pi\xi}{b}\right) \cos 4\pi \quad (1.9)$$

in which μ is the shear modulus, ν is the Poisson ratio, $\xi = \frac{a}{2(1-\nu)}$ is the parameter measuring the width of a dislocation (a is the lattice constant), b is the Burgers vector, and μ is a parameter for translation of the dislocation with certain distance, μb , from the original equilibrium position. With the combination of the relationship between EWF and Young's modulus as shown in Eq. (1.8), the correlation between the yielding strength and the electron work function was obtained:

$$\sigma_y = \frac{\alpha \exp\left(-\frac{4\pi\xi}{b}\right)}{1-\nu^2} \bar{m} \frac{18 \times 16^6 \pi^{10} \hbar^6 \varepsilon_0^9}{e^{16} m^3} \varphi^6 \quad (1.10)$$

As shown, like Young's modulus, the yield strength also has a sixth-power dependence on EWF. Besides, it is also influenced by the operation of slip systems related to applied stress orientation (\bar{m}), Poisson's ratio, Burger's vector, and the dislocation width (ξ).

1.1.4.7 Electron work function and hardness

Hardness is the resistance of a solid to plastic deformation during indentation. Although hardness is an integrated property of many fundamental mechanical properties such as the elastic stiffness, plasticity, strength and toughness, it is approximately proportional to the yield strength, as described as [40]

$$H = c\sigma_y \quad (1.11)$$

where c is a coefficient that depends on the materials and indenter geometry. Combing Eqs. (1.10) and (1.11), the correlation between the hardness and the electron work function can be obtained:

$$H = c\sigma_y = c \frac{\alpha \exp\left(-\frac{4\pi\xi}{b}\right)}{1 - \nu^2} \bar{m} \frac{18 \times 16^6 \pi^{10} \hbar^6 \varepsilon_0^9}{e^{16} m^3} \varphi^6 \quad (1.12)$$

1.1.4.8 Electron work function and number of transferred electrons

As explained in section 1.1.2, when two different materials are in electric contact with each other, their Fermi energies should be continuous across the junction, which requires a transfer of charges from the material with lower EWF to the material with higher EWF to achieve a thermodynamic equilibrium. The relationship between the number of transferred electrons and EWF can be expressed as follows [31]:

$$\Delta N = \Delta\varphi / \sum E_g^{AV} \quad (1.13)$$

Here ΔN is the number of transferred electrons, $\Delta\varphi$ is the difference of electron work function, and $\sum E_g^{AV}$ is average energy gap which is the difference in energy between the bottom of the conduction band and the top of the valence band.

1.1.4.9 Electron work function and electrode potential

An electric potential difference can be developed between the metal and the solution when a piece of metal is placed in an electrolyte solution, due to the charge transfer to equalize the Fermi level, which is very similar to what occurs when two dissimilar metals are placed in contact (electric) as mentioned above [41, 42]. The relationship between EWF and the electrode potential (E^M) can be expressed as:

$$E^M = \frac{\varphi_0^M}{e} + \delta\chi_\sigma^M - g^{s^*}(dip)_\sigma + g_{s^*}^M(ion)_\sigma - E_T(ref) \quad (1.14)$$

where φ_0^M is the electron work function of a clean metal surface and $\delta\chi_\sigma^M$ is the modification as metal M is brought in contact with solution s^* (electronic term), $g^{s^*}(dip)$ is the contribution due to any preferentially orientated solvent molecules (dipolar term), and $g_{s^*}^M(ion)$ is the additional potential drop due to the presence of free charges on either sides of the interface (molecule term). $E_T(ref)$ is the potential barrier at the reference electrode and is known as the “absolute potential” of the reference electrode [43].

1.2 General introduction to the Cu-Ni binary system

The Cu-Ni alloy system is commonly used as an example of a system which exhibits simple solid solution alloy behavior [44]. Except for a reported discovery of miscibility gap at low temperature [45], this system has complete solid solubility, which can be attributed to the fact that both copper and nickel are f.c.c. metals, and that their lattice parameters are similar as expected from their similar electronic structures and their adjacent positions in the periodic table. Therefore, Cu-Ni alloy system, an example as an isomorphous solid solution, is chosen in this study to eliminate the influence of second phases.

Cu-Ni alloys have been widely used in marine hardware, heat exchangers (Fig.1.2(a)), pipe work (Fig.1.2(b)), condensers in sea water systems, sheathings of ship's hull (Fig.1.2(c)), as well as desalinization equipment (Fig.1.2(d)), due to their high resistance to corrosion in the marine environment and other briny solutions [46]. Cu-Ni based alloys are also popular for bearing applications [47] (Fig.1.2(e)) under specific conditions especially when high thermal and electrical conductivities are required. Besides, because of their combination of wear and corrosion resistance, physical properties and ability to be coined, copper-nickel alloys are also widely used for coinage (Fig.1.2(f)).



(a) Heat exchanger



(b) Pipes



(c) Sheathing of hull



(d) Desalinization equipment



(e) Bearing applications



(f) Coin

Figure 1.2 Some applications of Cu-Ni alloys

1.3 Correlation between the wear resistance of Cu-Ni alloy and its EWF

Wear is defined by the American Society for Testing and Materials (ASTM) as the damage to a solid surface, generally involving the progressive loss of material, due to relative motion between two surfaces in contact [48]. Wear may also occur when the surface of engineering materials are in relative rolling motion [49]. When applied in conditions such as bearings abovementioned, good wear-resistance is required for Cu-Ni alloys.

Mechanical properties of materials and other related properties such as the tribological behaviors are largely dependent on their electronic structure or electron behavior, which governs the atomic bond strength. As mentioned in section 1.1.4.5-1.1.4.7, a correlation between material's mechanical properties and its electron work function has been established. However, whether such a correlation is applicable to alloys is less clear. Besides, the correlation between EWF and alloy's wear resistance is worth being investigated for understanding wear phenomena on a more fundamental base. It must be indicated that mechanical properties, thus wear resistance of materials are strongly affected by their microstructure, which complicates the dependence of the properties on the electron behavior. However, according to the recent studies [36, 50, 51], it appears that mechanical properties of a material are more or less governed by its overall EWF, which is linked to the roles that individual phases and interphase boundaries play in determining the properties. Such

dependence is more obvious for homogeneous alloys such as isomorphous Cu-Ni alloys. In this initial stage of exploring links between EWF and tribological phenomena, using Cu-Ni alloy system as a sample system, we are focused on isomorphous solid solutions without involvement of second phases. The objectives of this part of the study are 1) to investigate EWF, mechanical and tribological properties of Cu-Ni alloy with different concentrations of Ni, and 2) to correlate EWF with hardness, Young's modulus, sliding wear and erosion resistances of the material, and clarify mechanisms behind.

1.4 Correlation between the corrosion and corrosive wear resistance of Cu-Ni alloys and its EWF

Corrosion is defined [52] as the destructive attack of a metal by chemical or electrochemical reaction with its environment. Corrosion resistance or polarization behavior of materials is related to their chemical stability, which can be evaluated by their electron stability that is reflected by the electron work function. Since EWF reflects the difficulty for changing the electronic state of the solid, it could be taken into account when analyzing corrosion behavior of materials [4, 53, 54]. A higher work function corresponds to a more stable electronic state and thus a higher resistance to corrosion. However, when evaluating the nobility and corrosion behavior of materials, the electrode potential (E^M) or electrochemical series is frequently used to characterize material's activity or inertness. The electrode

potential is useful as an indicator of likely reactions leading to corrosion. An electropositive element will displace a less electropositive element from a solution of its ions. However, this parameter is environment-dependent and affected by surface adsorption and oxidation. Thus, misleading judgment could be resulted when determine the intrinsic nobility of element using the electrochemical series.

Numerous efforts have been made to investigate the corrosion behavior of Cu-Ni alloys. For instance, it was reported that [55] that 90-10 copper-nickel alloys are considered to be more susceptible to flow influenced corrosion than the 70-30 copper-nickel range of alloys and, for the lower nickel alloy-types, seawater velocities are usually limited to 3.5 ms^{-1} for pipe diameters $> 100 \text{ mm}$. Stewart and Popplewell [56, 57] observed that the addition of nickel increased impact toughness, corrosion resistance and high temperature strength relative to copper. And this improvement in corrosion resistance was generally attributed to the modification of aged surface oxide layers. Considerable studies on the correlation between the electron work function of materials and their various properties [18, 25, 36, 58, 59] have been conducted. For this part of study, Cu-Ni alloys were used as sample materials with the objectives of 1) analyzing and demonstrating the role of EWF in determine the material activity, and 2) providing complementary clues for corrosion-resistant material selection and design.

When the chemical attack is accompanied by physical deterioration, such as corrosive wear, the rate of material loss can be very high. The corrosion-wear synergy

plays an important role in attacking many industrial facilities when exposed to wear in corrosive environments. Typical examples are slurry pumps used in the oil sand industry, orthopedic implants, food processing facilities and mining equipment [60-62]. During corrosive wear, plastic deformation makes the target surface more anodic and thus accelerates material dissolution [63, 64]. On the other hand, corrosion degrades the surfaces in the form of pitting, brittle oxides or porous layers. The changes in surface structure in corrosive media decrease the resistance to mechanical attack and as a result, wear is accelerated by corrosion. Such synergistic attack of corrosion and wear can result in a higher rate of material removal. The interaction between corrosion and wear has found beneficial applications in the semi-conductor industry, such as the chemical-mechanical planarization (CMP) of interconnects for multilayer metallization in advanced integrated circuits [65].

The synergistic effect of mechanical and electrochemical actions on material loss during corrosive wear has drawn the interest of many researchers. Schmutz and Frankel [66] used AFM as a scratching device to locally remove the passive film on aluminum alloys. Jiang [67] investigated the effect of wear on corrosion of austenitic stainless steel in a sulfuric acid solution using a pin-on-disc apparatus. He then pointed out that the effect on wear on corrosion was found to be related to the recovery rate of passive films broken by scratching, and that the addition of wear can cause a negative shift in corrosion potential and an increase in corrosion current. This perspective is in good consistence with other researchers' work as mentioned above.

Quantitatively speaking, during corrosive wear, the total volume loss rate (r_{total}) includes three components, which are the rates of volume losses caused respectively by pure wear (r_w), pure corrosion (r_{corr}) and their synergistic attack (r_{syn}) [63, 64]. The total wear volume loss rate is expressed as:

$$r_{total} = r_w + r_{corr} + r_{syn} \quad (1.15)$$

The wear-corrosion synergy consists of two parts, the increase in wear rate due to corrosion (r_{c-w}) and the increase in corrosion rate due to wear (r_{w-c}):

$$r_{syn} = r_{c-w} + r_{w-c} \quad (1.16)$$

Understanding that material's both wear resistance and corrosion resistance are intrinsically dependent on its EWF, it is promising for us to use this fundamental parameter to characterize the corrosion-wear synergy.

1.5 Dependence of erosive wear on temperature via the electron work function

Many properties of materials are strongly affected by temperature. This is probably related to the influence of temperature on the behavior of electrons. Electron work function is temperature dependent [68, 69].

According to the Lennard-Jones potential, the potential between two atoms can be expressed as [70, 71]:

$$V(r) = \varepsilon_b \left[\left(\frac{r_e}{r} \right)^{12} - 2 \left(\frac{r_e}{r} \right)^6 \right] \quad (1.17)$$

where ε_b is the maximum value for the depth of the potential well, r is the distance between the two atoms and r_e is the equilibrium distance. It has been shown that the electron work function is related to the bond energy [71], which is shown as

$$\varphi(r_e) = C \varepsilon_b^{\frac{1}{6}} \quad (1.18)$$

where $\varphi(r_e)$ is the work function at equilibrium and C is a constant of proportionality. Since $V(r_e) = -\varepsilon_b$,

$$V(r_e) = -\frac{1}{C} \varepsilon_b^{\frac{5}{6}} \varphi(r_e) \quad (1.19)$$

The atomic displacement or vibration, Δr , is within a small range ($\Delta r = r - r_e$ and is smaller than $0.1 r_e$, otherwise the bond would become unstable [72]), so we have

$$V(r) = -\frac{1}{C} \varepsilon_b^{\frac{5}{6}} \varphi(r) \quad (1.20)$$

Combining this with Eq (1.17), the expression for the work function is finalized as

$$\varphi(r) = -\varphi(r_e) \left[\left(\frac{r_e}{r} \right)^{12} - 2 \left(\frac{r_e}{r} \right)^6 \right] \quad (1.21)$$

Letting $x = \frac{\langle r - r_e \rangle}{r_e}$, $\varphi(r)$ can be written as

$$\varphi(r) = -\varphi_0 [(1+x)^{-12} - 2(1+x)^{-6}] \approx \varphi_0 - 36x^2 \varphi_0 \quad (1.22)$$

The distance between the two atoms, i.e. the bond length, is affected by temperature. To clarify the $\varphi - T$ relationship, we have to firstly build the relation

between the bond length and temperature. The change in potential energy is similar to that in work function, and the temperature-dependent x varies as [71] $x = \frac{1}{r_e} \frac{3g}{4f^2} k_B T$, where we have $g = 252 \frac{\varphi_0}{r_e^3}$ and $f = 36 \frac{\varphi_0}{r_e^2}$. Thus x becomes

$$x = \left(\frac{7}{48} \frac{k_B T}{\varphi_0} \right) \quad (1.23)$$

Combining Eqs. (1.22) and (1.23), we have

$$\varphi(T) = \varphi_0 - 36 \left(\frac{7}{48} \frac{k_B T}{\varphi_0} \right)^2 \varphi_0 \quad (1.24)$$

Considering the potential due to the interaction of other adjoining atoms, this expression can be generalized for solids. The term $36x^2\varphi_0$ can be described as:

$$36\varphi_0 \sum_{i=1}^N w_i \left(\frac{\langle r_i - r_{e1} \rangle}{r_{ei}} \right)^2 = \xi \varphi_0 \left(\frac{r_1 - r_{e1}}{r_{e1}} \right)^2 = \gamma \varphi_0 \left(\frac{k_B T}{\varphi_0} \right)^2 \quad (1.25)$$

where $\langle r_i - r_{e1} \rangle$ represents the average deviation of atom i away from the equilibrium position (chosen as the origin). w_i is an energy contribution factor that counts the influence of the i th neighbor atom on the square of relative oscillation amplitude, x^2 . This contribution factor is distance-dependent, e.g., from the Lennard-Jones potentials, the contributions from the nearest neighbour, 2nd and 3rd neighbour atoms are $w_{r_e} = 1$, $w_{2r_e} = 3.1 \times 10^{-2}$ and $w_{3r_e} = 2.7 \times 10^{-3}$, respectively. $\varphi(T)$ can thus be expressed as

$$\varphi(T) = \varphi_0 - \gamma \frac{(k_B T)^2}{\varphi_0} \quad (1.27)$$

Since the values for work function are available at room temperature (i.e. 295K), the relationship for the work function can be adjusted as

$$\varphi(T) = \varphi_{295} - \gamma \frac{(k_B \tau)^2}{\varphi_{295}} \quad (1.28)$$

in which $\tau = T - 295$. γ can be written as $\gamma = \xi \left(\frac{7}{48}\right)^2$ and ξ is:

$$\xi = \frac{36}{\chi_1^2} \sum_{i=1}^N \left(\frac{\langle r_i - r_{e_1} \rangle}{r_{e_1}} \right)^2 \quad (1.29)$$

where $\chi_1 = \frac{\langle r_i - r_{e_1} \rangle}{r_{e_1}} = \alpha_L T$ and α_L is the linear thermal expansion coefficient

of metal. Considering the periodicity of the lattice, we have:

$$r_{e_i} = r_{e_1} + (i - 1)a \quad (1.30)$$

a is the lattice parameter and r_{e_1} is the nearest neighbour distance, which equals $\frac{a}{\sqrt{2}}$ for f.c.c. crystals and $\frac{\sqrt{3}a}{2}$ for b.c.c. crystals, respectively. Thus, for face-centred cubic metals, we have:

$$\xi_{fcc} = \frac{36}{\chi_1^2} \sum_{i=1}^N w_i \left(\frac{\chi_1 + \sqrt{2}(i - 1)}{1 + \sqrt{2}(i - 1)} \right)^2 \quad (1.31)$$

Similarly, for b.c.c. metals we have:

$$\xi_{bcc} = \frac{36}{\chi_1^2} \sum_{i=1}^N w_i \left(\frac{\chi_1 + \frac{2}{\sqrt{3}}(i - 1)}{1 + \frac{2}{\sqrt{3}}(i - 1)} \right)^2 \quad (1.32)$$

Chapter 2

Correlation Between the Wear Resistance Of Isomorphous Cu-Ni Alloy And Its Electron Work Function

2.1 Objectives

The objectives of this part of study are 1) to investigate EWF, mechanical and tribological properties of Cu-Ni alloy with different concentrations of Ni, and 2) to determine how the wear resistance of the alloy is reflected by its work function and clarify the mechanisms behind.

2.2 Experimental procedures

Table 2.1 gives compositions of prepared samples. Pure copper (99.9 wt. %) and pure nickel (99.9 wt. %) provided by Strem Chemicals were melted together with different ratios using an arc melting furnace. The formed Cu-Ni alloys are homogeneous solid solutions. In order to minimize possible compositional inhomogeneity, all the samples were melted at least three times and annealed in argon atmosphere at 600 °C for 3h and slowly cooled down in the furnace. The samples were ground with 400#, 600#, 800# and 1200# silica papers and finally polished using 1 μm diamond suspension. Figure 2.1 illustrates SEM images of three representative Cu-Ni samples. As shown, the samples are homogeneous without presence of second phases. Thus, measured work functions represent the overall values of the isomorphous alloy samples.

Table 2.1 Compositions of the Cu-Ni alloys made for the study.

Sample NO.	Cu content (wt. %)	Ni content (wt. %)
#1	100	0
#2	95	5
#3	90	10
#4	80	20
#5	50	50
#6	20	80
#7	10	90
#8	0	100

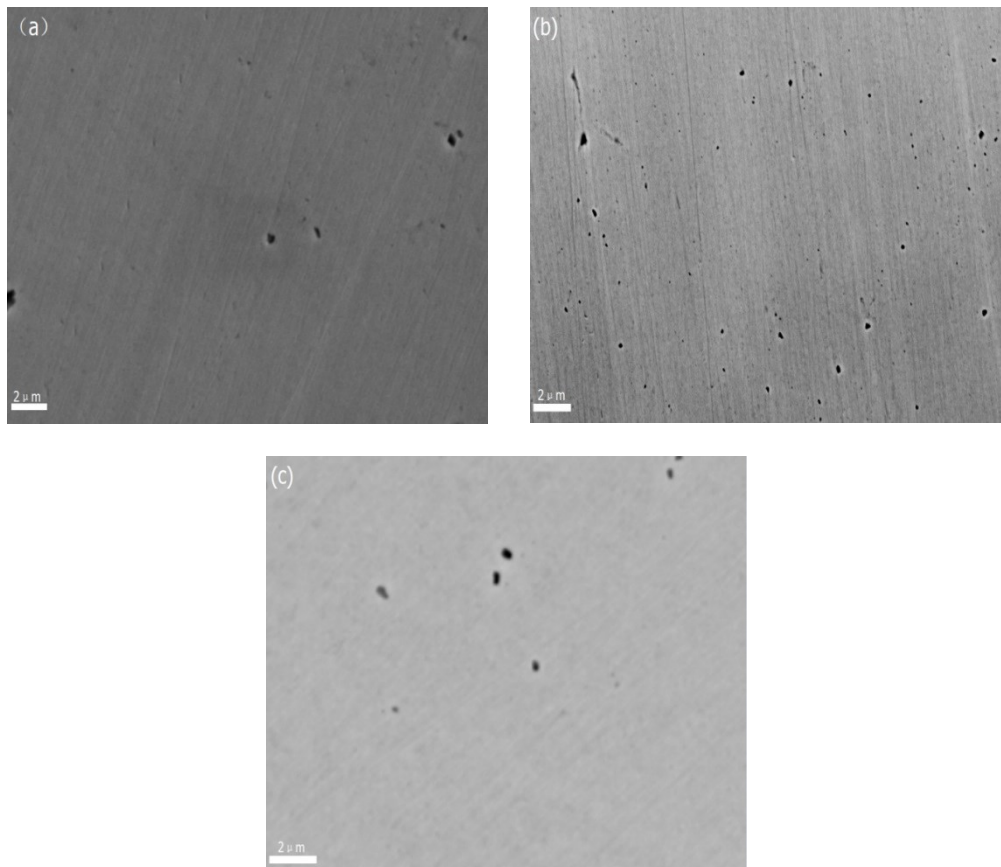


Figure 2.1 SEM backscattered images of samples (a) 80Cu-20Ni, (b) 50Cu-50Ni and (c) 10Cu-90Ni.

EWFs of the samples were measured with Ultraviolet Photoelectron Spectroscopy (UPS), which is used to analyze the kinetic energy distribution of the emitted photoelectrons and study the composition and electronic state of the surface region of a sample. From the onset of photoelectron emission, one can measure the work function, which is determined by subtracting energy of the onset of photoelectron emission from the photon energy. In this study, an AXIS Ultra DLD was used to collect EWF data. Samples were bombarded with an unfiltered He (21.2 eV) excitation source and the corresponding secondary cut-off was recorded. The pass energy of the instrument was 5 eV and a 110 μm aperture was used to collect light. All samples were sputtered by argon ions for 4 min to remove possible adsorbed substances on surface before the EWF measurement. The instrument was operated in ultrahigh vacuum of 3×10^{-8} Torr. Young's modulus and hardness of the alloys were measured using a micro-indenter. A cone-shaped indenter tip was used and the load was applied to the indenter at a loading rate of 15mN/s. Values of hardness and Young's modulus were obtained automatically from the load-indentation depth curve. Each presented value is an average of at least 10 measurements at different locations on each sample. The sliding wear tests were performed on a pin-on-disc tribometer (CSEM Instruments CH-2007, Neuchatel, Switzerland). The disc was the sample and the pin was a silicon nitride ball with a diameter equal to 3 mm. All sliding tests were performed at a sliding speed of 2 cm/s along a circle path of 2.0 mm in diameter under a normal load of 2 N for 10,000 rotations, corresponding to a total sliding distance of 62.8 m. Each wear test was repeated at least three times. Wear tracks

were observed under an optical confocal microscope (Zeiss Axio CSM700, Jana, Germany) and the volume loss was then calculated. A home-made air-jet erosion tester was used to perform solid-particle erosion tests. The pressure of the air flow was kept constant at 40 psi to eject sand particles, corresponding to a sand particle velocity of 55 m/s. Three different impingement angles were used for the tests: 45°, 60° and 90°. 2125 g fine sand (AFS 50-70) was consumed for every test. The air and sand mixture was delivered through a nozzle of 4 mm in inner diameter and the distance between the nozzle and samples was 20 mm. A balance with an accuracy of 0.1 mg was used to determine the weight loss by weighting each specimen before and after test. Both sliding wear tracks and eroded surfaces of the alloys were examined using a Vega-3 TESCAN Scanning Electron Microscope at 20 kV and an EDXS oxford instrument was employed to analyze local compositions of different domains.

2.3 Results and discussion

2.3.1 EWF measurement

The electron work functions of samples with different compositions were determined from obtained UPS spectra. Figure 2.2 presents EWF values with respect to the concentration of Ni (wt.%). As shown, the work function generally increases with an increase in the concentration of Ni. The increase in work function with %Ni is explainable. The work function is related to the “free” electron density. For a homogeneous solid solution, A_xB_{1-x} , its work function (φ_{AB}) is expressed as [23]:

$$\varphi_{AB} \propto n_{AB}^{1/6} \approx 7.8 n_{AB}^{1/6} = 7.8 \frac{z_{AB}^{1/6}}{a_{AB}^{1/2}} \quad (2.1)$$

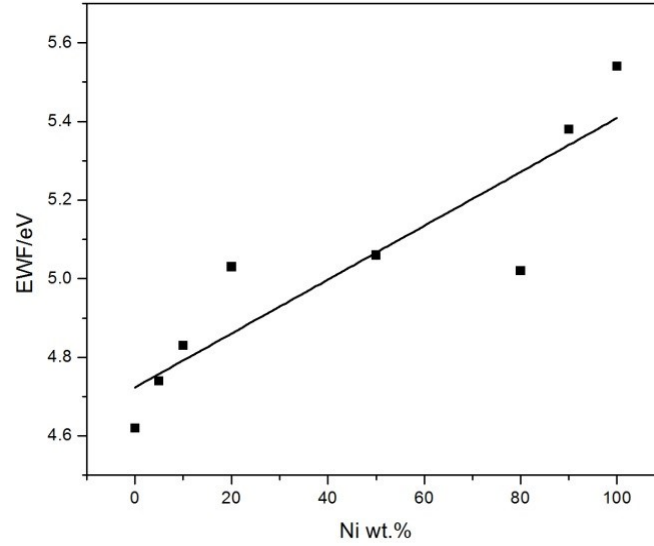


Figure 2.2 Electron work functions of the fabricated alloys measured with UPS.

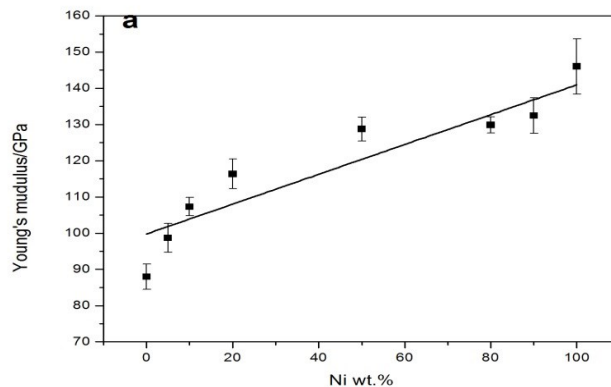
where z_{AB} is the valence number of the alloy and n_{AB} is the corresponding “free” or valence electron density. a_{AB} is the lattice constant of the alloy. For binary solid solutions, the overall work function can be expressed as [51]:

$$\varphi_{AB}^6 \approx X_A \varphi_A^6 + X_B \varphi_B^6 \quad (2.2)$$

where φ_A and φ_B are work functions of elements A and B. Since Ni has a higher work function ($\varphi_{Ni} = 5.15eV$) than Cu ($\varphi_{Cu} = 4.6eV$), adding Ni to Cu increases the overall work function.

2.3.2 Correlation between EWF and Young's modulus and Hardness

Figures 2.3(a) and 2.3(b) illustrate Young's modulus and micro-hardness versus %Ni for the samples, respectively. It is clear that both the two mechanical properties are enhanced with an increase in the amount of added Ni, corresponding to an increase in EWF as illustrated in Fig.2.2. This indicates clear correlations between the mechanical properties and the electron work function, which has been demonstrated in previous studies [50]. When Ni having a higher EWF is added to Cu, the density of free electrons in the material increases, resulting in a rise in the electrostatic interaction between electrons and positive nuclei. As a result, the average strength of atomic bond is elevated, which is responsible for the increase in Young's modulus. The stronger atomic bond also raises the barrier to generation and movement of dislocations, thus an increase in hardness can be achieved. Although both EWF and Young's modulus have a similar trend with respect to the nickel concentration in our study (increase as Ni concentration increases), one important advantage of EWF over Young's modulus is that one may select a particular element to modify material's mechanical properties based on element's EWF.



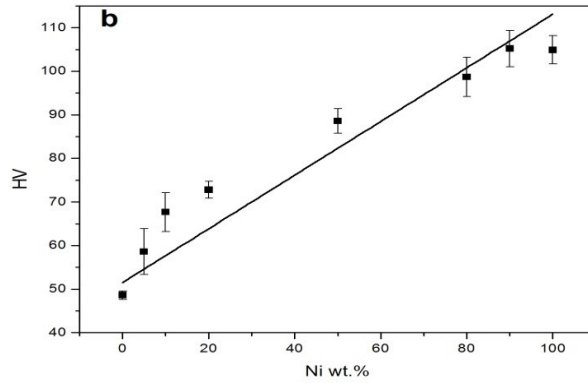


Figure 2.3 Young's modulus (a) and hardness (b) of the fabricated Cu-Ni alloys.

2.3.3 Resistance to sliding wear and its relation with EWF

The relationship between material's hardness and sliding wear loss generally follows Archard's equation [73]:

$$WL = K_w \frac{F \cdot l}{H} \quad (2.3)$$

where WL is the material volume loss during wear process, F represents the normal load applied to the worn surface, l is the sliding distance. H is the hardness of the material. K_w is a wear coefficient.

Attempts have been made to establish a correlation between hardness and electron work function, which has the following form [50]:

$$H \propto \varphi^6 / (1 - \nu^2) \quad (2.4)$$

Combining Eqs. (2.3) and (2.4) yields

$$WL = K_w \frac{F \cdot l}{H} \propto \frac{F \cdot l (1 - \nu^2)}{\varphi^6} = K_{w\varphi} \frac{F \cdot l (1 - \nu^2)}{\varphi^6} \quad (2.5)$$

This equation suggests a reverse sextic relation between the sliding wear loss and work function of the target material. We may use a coefficient, $K_{W\phi}$, to replace K_W when the hardness is represented by the work function .

Volume losses of the Cu-Ni samples during sliding wear were measured and are presented in Fig.2.4. As illustrated, samples with higher Ni concentrations show larger wear volume losses in the ambient environment, despite their higher hardness. This is opposite to our expectation based on Eq.(2.5). To understand this unexpected observation, we examined worn surfaces of the samples.

Figure 2.5 and Table 2.2 illustrate worn surface morphologies and compositions of the samples, respectively. As shown, considerable oxidation was observed on the worn surface of a pure Cu sample and the oxide scale fully covered the wear track. The oxide scale appeared to be compacted and adhered to the substrate. Such an oxide scale was hard to be removed during sliding wear process and thus acted as a protective coating to prevent further wear of the material. There is a distinctive morphological difference in worn surface between a pure Ni sample (see Fig.2.5 (b)) and the Cu sample, although EDS analysis showed that the oxygen content was also high on the worn surface of the Ni sample. The wear debris is turned out to be NiO, which is brittle in nature [44]. Under the wearing force, it could be removed with less difficulty, thus facilitating wear damage to the Ni sample. Plowing is an obvious characteristic of the worn surface of the Ni sample. Worn surface of

sample 50Cu-50Ni showed a mixed character: both the oxide scale fragments and plowing track can be observed.

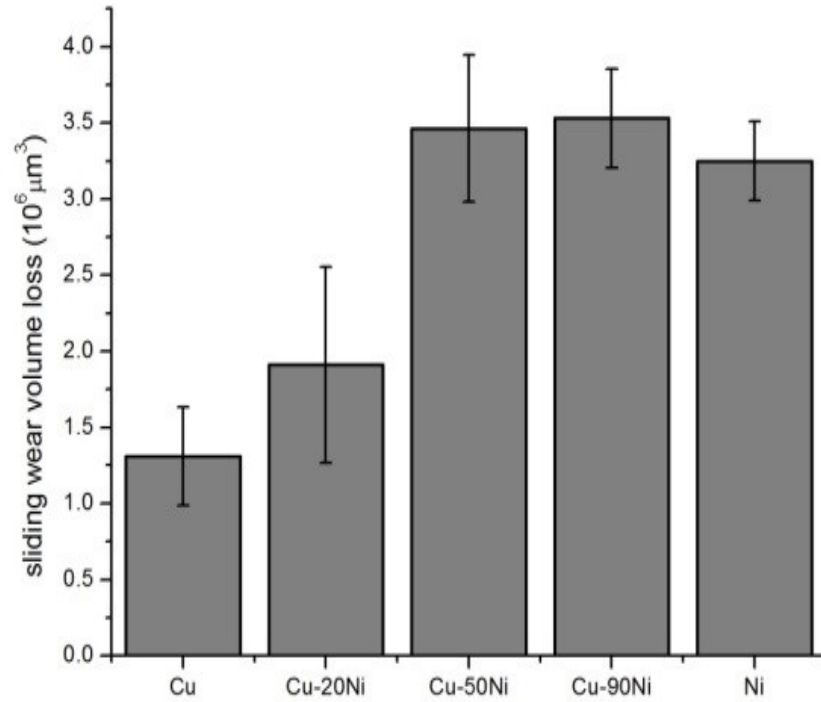


Figure 2.4 Sliding wear loss of Cu-Ni samples with different concentrations of Ni.

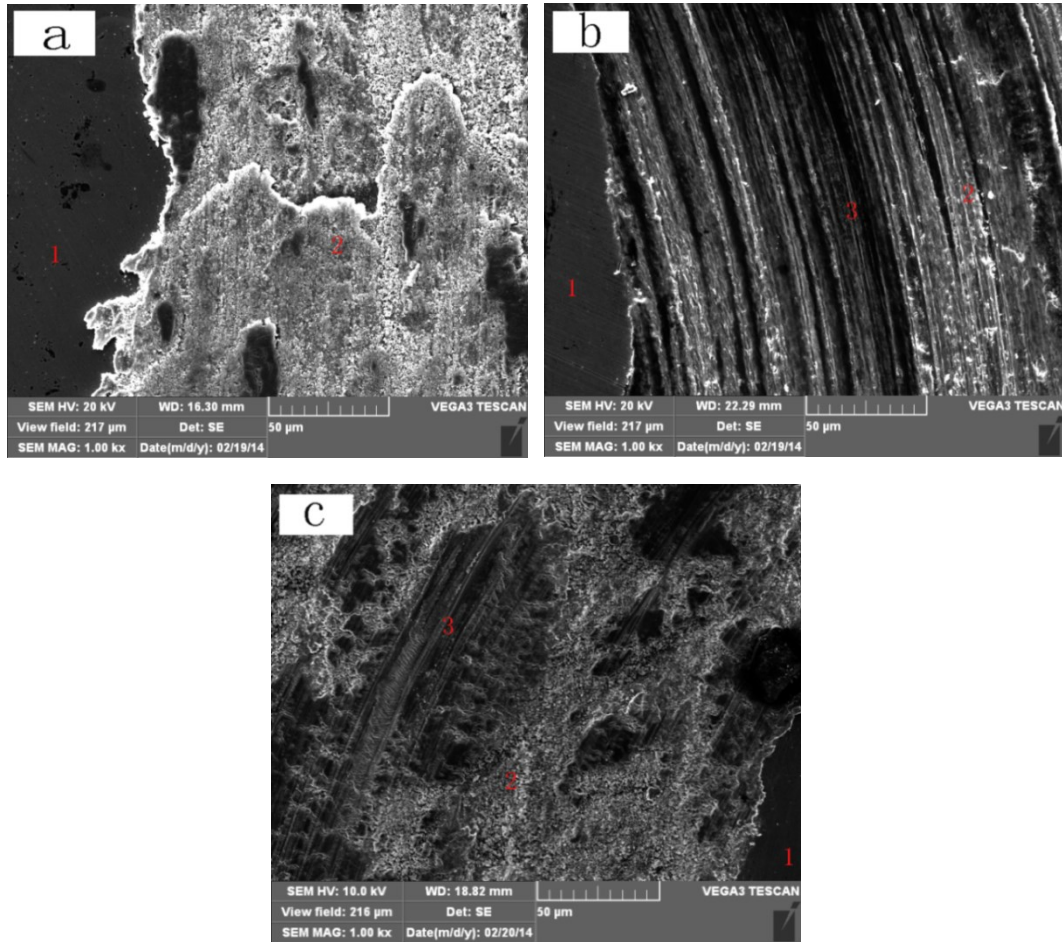


Figure 2.5 SEM images of worn surface of three selected alloys. (a) Cu, (b) Ni, and (c) 50Cu-50Ni.

Table 2.2 -Spot Energy Dispersive Spectroscopy (EDS) analysis of Cu, Ni and 50Cu-50Ni after sliding wear.

Sample		Cu (at. %)	Ni (at. %)	O (at. %)
Cu (Fig.2.4-a)	Spot 1	95	-	5
	Spot 2	57	-	43
Ni (Fig.2.4-b)	Spot 1	-	98	2
	Spot 2	-	47	53
	Spot 3	-	34	66
50Cu-50Ni (Fig.2.4-c)	Spot 1	65	32	3
	Spot 2	22	17	60
	Spot 3	20	16	64

The composition analysis for the worn surfaces using EDS confirmed the formation of oxides (see Table 2.2). On the original surfaces of the three samples (spot 1 in Fig.2.5(a), (b) and (c)), the oxygen content was low. While considerable oxidation occurred on the wear tracks (all the other spots in Figure 2.5). Although the measurement of oxygen content with EDS may not be very accurate, the significant increase in the oxygen content is a clear indication of oxidation during the sliding wear process.

In order to confirm the influence of oxidation on both Ni and Cu, a flow of argon gas was introduced to the sample surface during the sliding wear process. Since the sample holder was not sealed to completely isolate it from air, the argon flow could only marginally minimize the exposure of sample to air. The argon flow might help lower the sample surface temperature (raised by frictional heat), but this could not be much since the sliding speed was not high. Thus, the influence of oxidation on wear could be alleviated only to a limited extent. However, even with the limited reduction of sample exposure to air, Cu already showed an increase in volume loss from $\sim 1.4 \times 10^6 \mu\text{m}^3$ (in air) to $\sim 1.9 \times 10^6 \mu\text{m}^3$, while that of Ni decreased from $\sim 3.1 \times 10^6 \mu\text{m}^3$ (in air) to $\sim 3.0 \times 10^6 \mu\text{m}^3$. Although the changes were small, the trend of changes was expected when oxidation was reduced.

In conclusion, the unexpected variation in the wear resistance of Cu-Ni alloy with respect to the Ni content was mainly attributed to the formation of oxide scales, which overwhelmingly influenced the effect of intrinsic hardness on the wear

resistance. Cu has a lower work function, corresponding to higher surface activity. This may promote the formation of oxide and the oxide/substrate adherence, thus leading to a protective role of the oxide scale in resisting wear. If the oxidation can be eliminated, the wear resistance should be largely reflected by the work function. This has been demonstrated in next section, in which results of solid-particle erosion tests are reported.

2.3.4 Resistance to solid particle erosion and its relation with EWF

If the oxidation can be eliminated, the wear resistance should be largely reflected by the work function, which is directly related to the material's Young's modulus and hardness. In this study, we performed solid-particle erosion tests. The high-speed sand flow would prevent the formation of an oxide scale or would not provide sufficient time for an oxide scale to develop on sample surface, thus minimizing the participation of oxidation in the erosion process. It should be indicated that high-speed solid particle erosion could raise sample surface temperature, leading to more or less oxidation. However, no an integrated oxide scale may stay on surface and play a protective role in the erosion process when the surface is eroded by a high-speed sand flow.

Figure 2.6 illustrates average volume losses of the samples during the air-jet solid-particle erosion tests at impingement angles of 30°, 60° and 90°, respectively. Mass losses of the samples were measured and then, for the purpose of comparison,

converted into volume losses by taking density into consideration. The density of Cu-Ni alloys is approximately determined as

$$\rho_{alloy} \approx X_{Cu}\rho_{Cu} + X_{Ni}\rho_{Ni} \quad (2.6)$$

where ρ_{Cu} and ρ_{Ni} are densities of copper and nickel, which are $\rho_{Cu}=8.96$ g/cm³ and $\rho_{Ni}=8.91$ g/cm³, respectively.

As shown, erosion wear loss decreases as the impingement angle increases within the current angle range (30°-90°). This is a normal trend for ductile materials. As demonstrated, the material loss decreased as the EWF of the alloy increased. This confirms the expectation that alloys with higher EWF can perform better in resisting wear without oxidation involved, due to the fact that a higher work function corresponds to a larger barrier to the attempt to change the electron state and other related states such as mechanical and electrochemical ones.

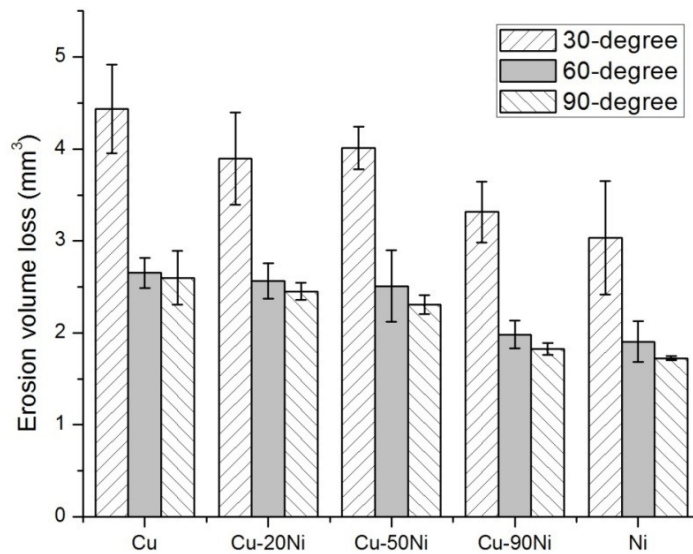


Figure 2.6 Erosion rates of the fabricated alloys with three impingement angles.

Eroded surfaces of the alloys were observed under SEM. Fig.2.7 illustrates surfaces of samples Cu, Ni and 50Cu-50Ni eroded at the impingement angle of 90°. As shown, there is no significant morphological difference among the three samples under study. Local composition analysis, as shown in Table 2.3, indicates a less severe oxidation condition compared with what we observed during the sliding wear tests. No obvious oxide scales are visible on the eroded surfaces. These confirm the expectation that oxidation is suppressed during the high-speed particle erosion tests. For the ductile materials, their hardness, which is related to its EWF, should play a predominant role in resisting the solid-particle erosion. No silicon signal was collected in the EDS analysis, which indicates that the particles imbedded in the target

materials during the erosion process have been scoured out and their influence on the weight loss measurement is thus negligible.

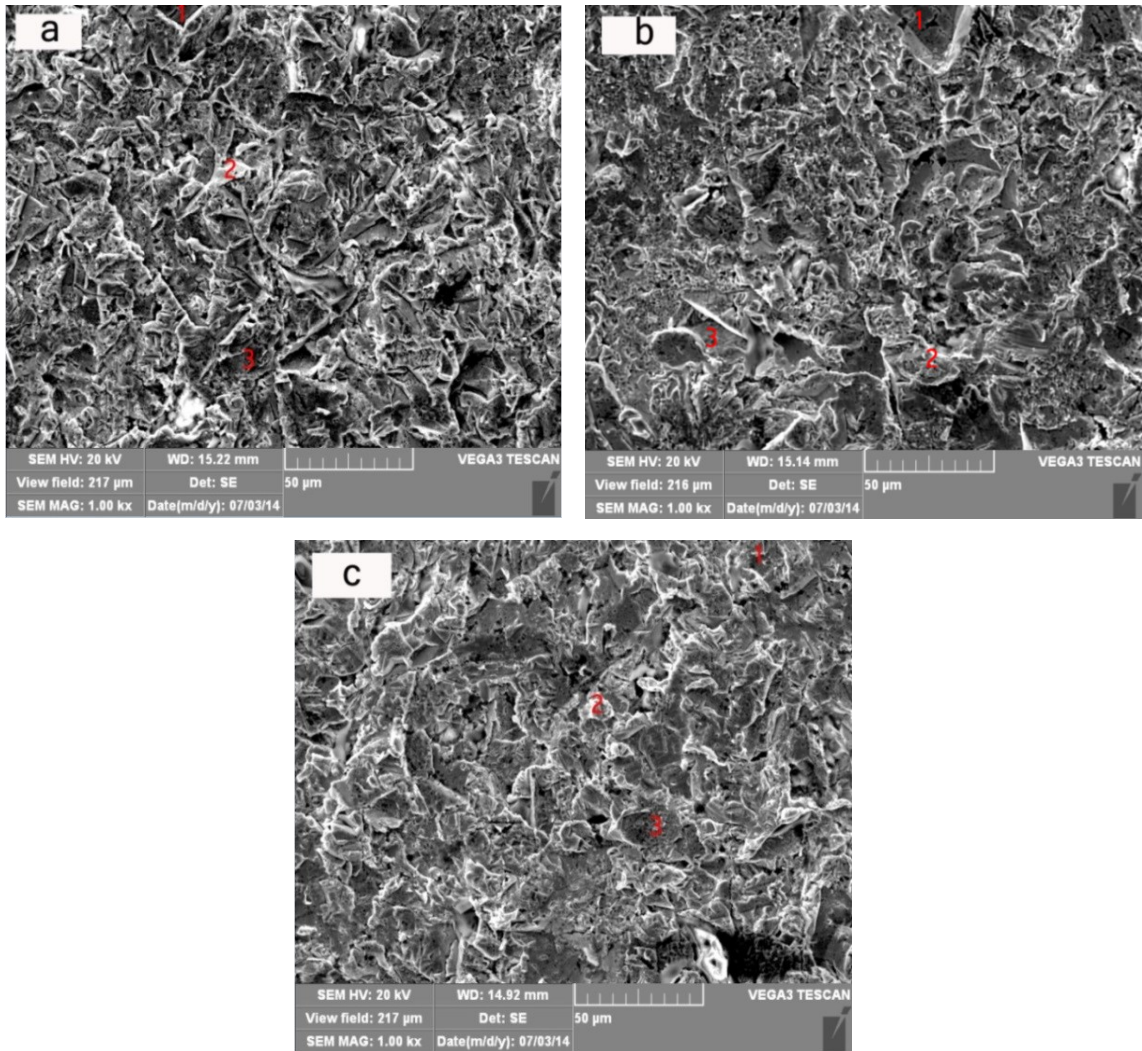


Figure 2.7 Eroded surfaces of three samples after erosion under the 90° air-jet solid particle erosion condition: (a) Cu; (b) Ni and (c) 50Cu-50Ni.

Table 2.3 - Spot EDS analysis of Samples Cu, Ni and 50Cu-50Ni after erosion.

Sample		Cu (at. %)	Ni (at. %)	O (at. %)
Cu (Fig2.6-a)	Spot 1	92	-	8
	Spot 2	88	-	12
	Spot 3	80	-	20
Ni (Fig2.6-b)	Spot 1	-	94	6
	Spot 2	-	93	7

50Cu-50Ni (Fig2.6-c)	Spot 3	-	87	13
	Spot 1	55	35	10
	Spot 2	37	33	30
	Spot 3	63	32	5

Attempts were made by the authors to establish the relation between the intrinsic erosion resistance and the work function for isomorphous solid solutions. For ductile materials [74] the contact area created by the impingement of particle, A_c , may be expressed as:

$$A_c \propto \frac{F}{H} \quad (2.7)$$

F represents the impact force. H is the hardness of the material. During erosion, the impact force comes from the kinetic energy of solid particle associated with its moment change when striking the target surface:

$$F = -m \frac{dv_y}{dt} \quad (2.8)$$

where m is the mass of the particle, and v_y represents the vertical component of the velocity of the particle. Thus we have

$$m \frac{dv_y}{dt} = -HA_c \quad (2.9)$$

$$m \left(\frac{dy}{dt} \right) \cdot dv_y = -HA_c \cdot dy \quad (2.10)$$

$$\therefore \int_v^0 m v_y dv_y = - \int_0^d HA_c dy = - \int_0^d HA_c(y) dy \quad (2.11)$$

If the particle strikes the surface at 90°, the above integration yields

$$\text{Indentation volume, } V = A_c \cdot d = \frac{mv_y^2}{2H} \quad (2.12)$$

If the particle strikes the surface at a certain angle, the horizontal velocity needs to be taken into account. Taking also the correlation between hardness and EWF as shown in Eq. (1.12), a general relation between the erosion volume loss (V) and material's hardness and thus the work function can be expressed as

$$V = K_E \frac{mv^2}{H} = K_{E\phi} \frac{mv^2(1-\nu^2)}{\phi^6} \quad (2.13)$$

where K_E is an erosion coefficient, which is related to the impingement angle of the particle and other factors such as the size and angularity of particle. When the hardness is converted to work function, this coefficient is replaced by $K_{E\phi}$.

Figure 2.8 illustrates measured erosion loss versus the work function for the five samples, which basically follow the proposed inverse sextic relation between erosion loss and the work function. As shown, the relationship between the erosion loss and work function is well demonstrated.

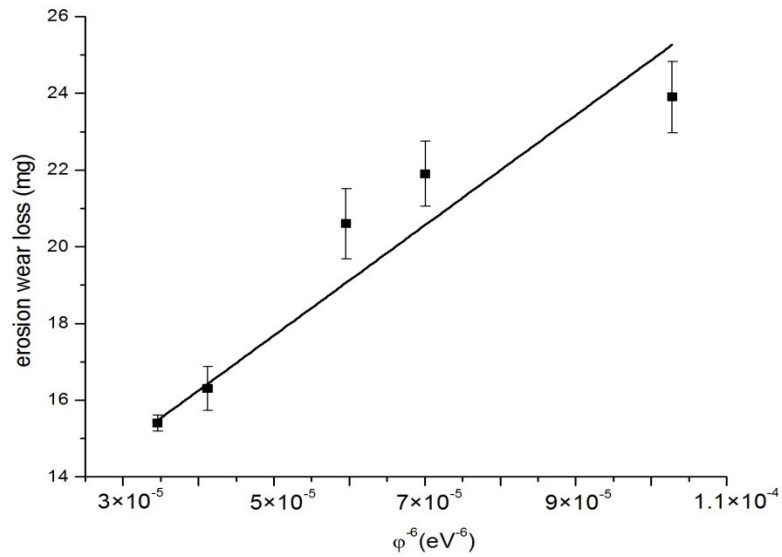


Figure 2.8 Erosion loss against the work function.

Up to this point, the proposed relationship between EWF and wear has been demonstrated to work for this isomorphous solid solution. Whether the relationship is also applicable to multiphase materials needs further studies on whether or not the overall EWF can appropriately reflect the integrated behaviour of the materials that are influenced by individual phases and interfaces.

2.4 Summary

Electron work function, mechanical behavior, sliding wear and solid-particle erosion of isomorphous Cu-Ni alloy with respect to the concentration of Ni were investigated. This chapter demonstrated that the EWF of the alloy increased with increasing its Ni concentration, leading to corresponding increases in Young's modulus and hardness. The enhancement of the mechanical strength raised the

resistance to solid-particle erosion. However, variations in the sliding wear resistance of the alloy with Ni concentration showed an opposite trend, which was turned out to be caused mainly by the formation of oxide scales which affected the sliding wear resistance differently when the Ni concentration was changed. This study demonstrates the correlation between the electron work function and tribological properties of the Cu-Ni alloys as well as the promise of using EWF as an alternative or supplementary parameter for tribo-material design.

Chapter 3

Correlation Between Corrosion Resistance, Corrosive Wear and EWF

3.1 Objectives

The objectives of this specific part of study are 1) to investigate the correlation between EWF, corrosion resistance as well as corrosive wear behaviors of Cu-Ni alloy with different concentrations of Ni, and 2) to demonstrate that the intrinsic nobility of a metal is ultimately governed by its electron stability, and that EWF could be regarded as a guiding parameter in corro-material design.

3.2 Experimental procedures

Same samples as described in section 2.2 were chosen in this part of study. EWFs, young's modulus and the hardness of the fabricated samples are shown in fig.2.2, fig.2.3(a) and fig.2.3(b), respectively.

Before the immersion tests, all the samples were cut with the same size and similar surface area, polished with #1200 sand papers. The immersion tests were performed for 7 days at room temperature in different solutions. The surface roughness of the immersed samples was then analyzed using a Zeiss's white light scanning confocal system (Zeiss Axio CSM700, Jana, Germany). After the immersion tests, the samples were rinsed in alcohol with an ultrasonic cleaner, dried with pressed air. Weight losses of pure Cu and pure Ni were measured with a balance with an accuracy of 0.1 mg.

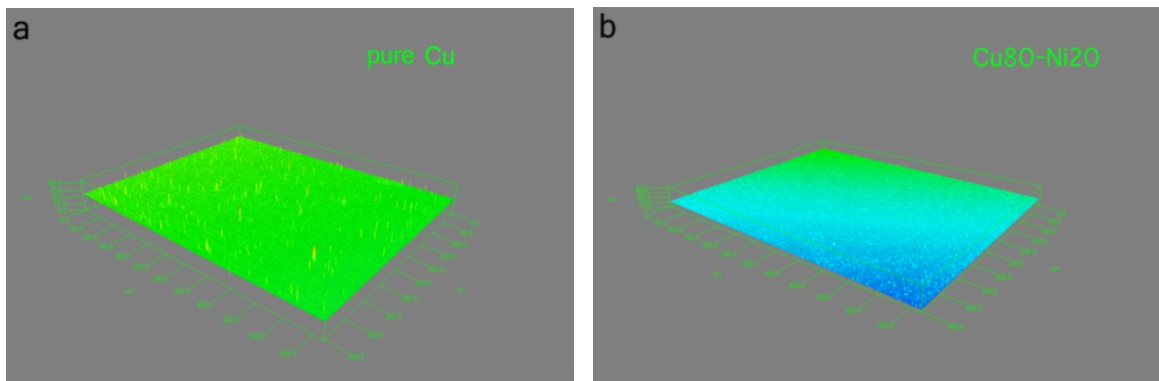
Corrosive sliding wear tests were performed using a pin-on-disc tribometer (CSEM Instruments CH-2007, Neuchatel, Switzerland) with a container, in which two

different corrosive media, NaCl solution (3 wt.%) and HCl solution (pH=3.0) were used, respectively. The disc was the sample and the pin was a silicon nitride ball with a diameter equal to 3 mm. All sliding tests were performed at a sliding speed of 2 cm/s along a circle path of 2.0 in diameter under a normal load of 2 N for 10,000 rotations. Each wear test was repeated at least three times. Wear tracks were observed under the Zeiss confocal microscope and the volume loss was then calculated. A home-made slurry jet erosion apparatus was used to perform the slurry erosion tests. The pressure of the air flow was kept constant at 30 psi to eject the slurry, which was composed of 2125g fine sand (AFS 50-70) and 300 mL 3 wt. % NaCl solution for each test. The air, sand and the corrosive medium mixture was delivered through a nozzle of 6 mm in inner diameter and the distance between the nozzle and the sample was about 20 mm. The impingement angle was fixed at 45°. A balance with an accuracy of 0.1 mg was used to determine the weight loss by weighting each specimen before and after test. Both sliding wear tracks and eroded surfaces of the alloys were examined using a Vega-3 TESCAN Scanning Electron Microscope at 20 kV and an EDXS oxford instrument was employed to analyze local compositions of different domains.

3.3 Results and discussions

3.3.1 Corrosion behavior

Figure 3.1 and Figure 3.2 illustrate changes in surface roughness of Cu-Ni samples after being immersed in stagnant NaCl (3 wt.%) and HCl (pH=3) solutions, respectively, for 7 days. The different colors correspond to different surface heights with respect to the reference surface selected before measurement (a deeper color corresponds to a greater surface roughness). As shown, all the five samples immersed in the NaCl solution have relatively smooth surfaces after the immersion tests. While in HCl, distinct differences were observed between the Cu-rich samples and those Ni-rich ones. The surfaces of Cu, 80Cu-20Ni and 50Cu-50Ni are rough, covered by some scales. The Ni and Ni-rich samples (#4 and #5) are relatively smooth. The surface roughness decreases with an increase in Ni concentration as Fig. 3.2 illustrates.



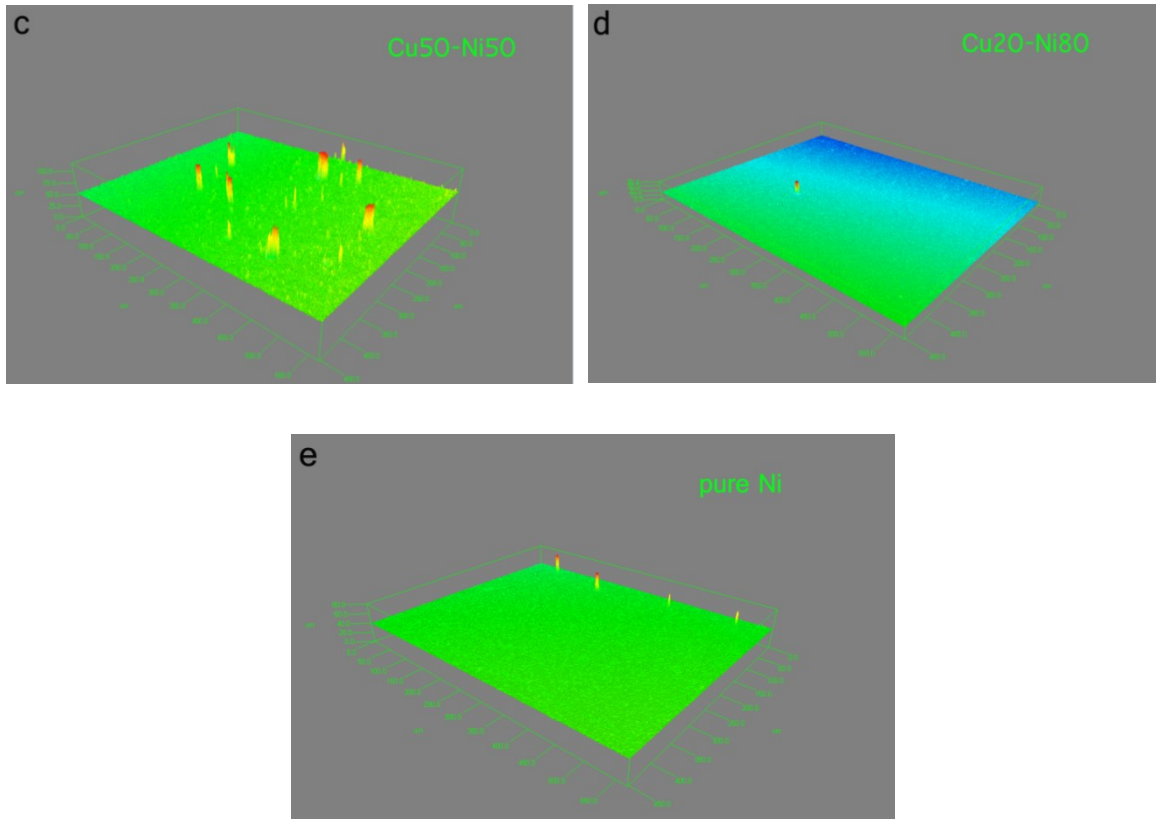
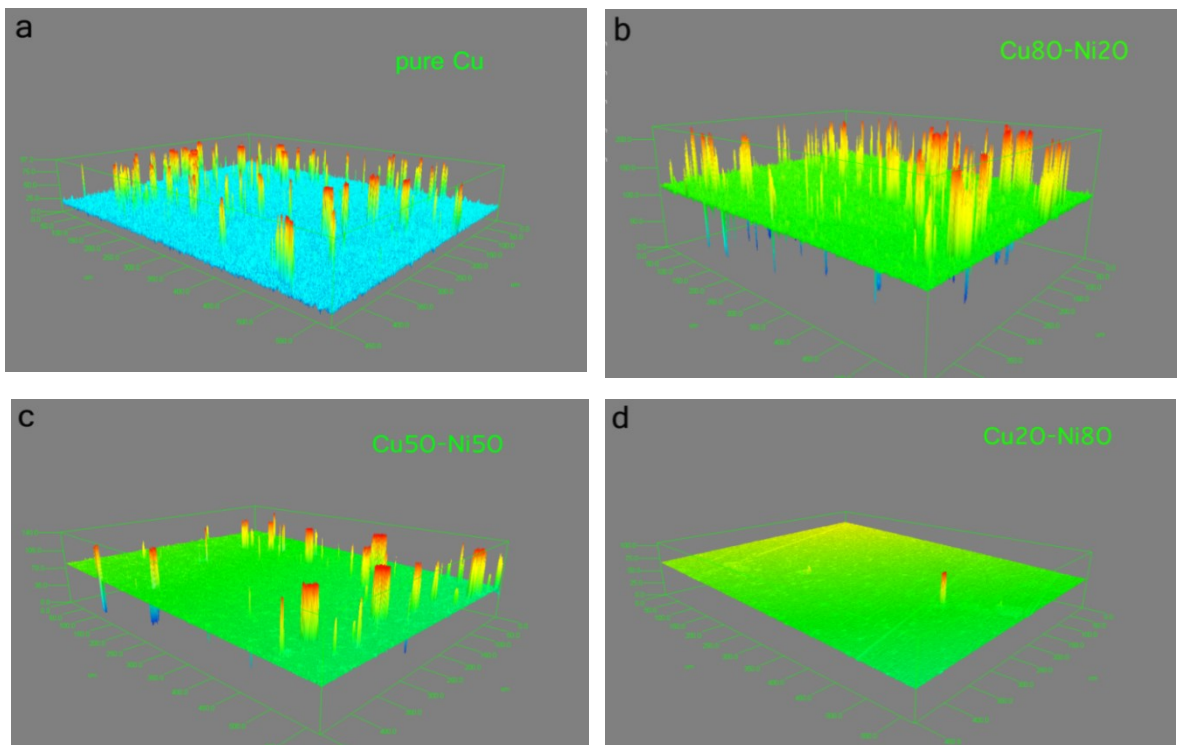


Figure 3.1 Surface roughness of samples after immersion in NaCl solution for 7 days. (a) Cu, (b) 80Cu-20Ni, (c) 50Cu-50Ni, (d) 20Cu-80Ni and (e) Ni.



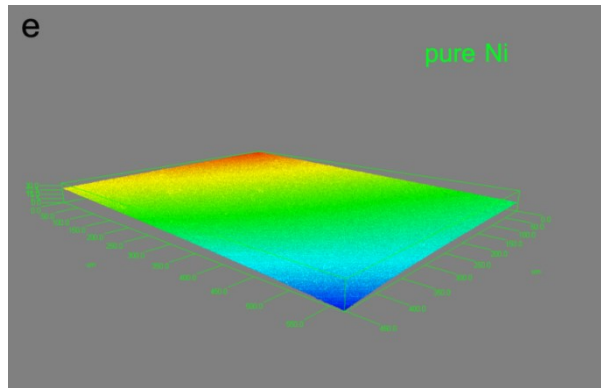


Figure 3.2 Surface roughness of samples after immersion in HCl solution for 7 days. (a) Cu, (b) 80Cu-20Ni, (c) 50Cu-50Ni, (d) 20Cu-80Ni and (e) Ni.

Figure 3.3 and figure 3.4 represent the morphologies of the samples after immersion in NaCl solution and HCl solution, respectively. Corresponding surface compositions were analyzed and are given in Table 3.1. As the SEM images have shown, all the samples have similar surface morphologies after immersed in the NaCl solution. This is consistent with the surface roughness measurement shown in Fig.3.1. While after immersion in the HCl solution, Cu-rich alloys have rough surfaces, especially pure Cu (#1); surfaces of samples containing higher Ni concentrations are less rough and the Ni sample (#5) is very smooth. This may indicate that adding Ni to Cu-Ni alloys improves material's resistance to corrosion in the acidic environment.

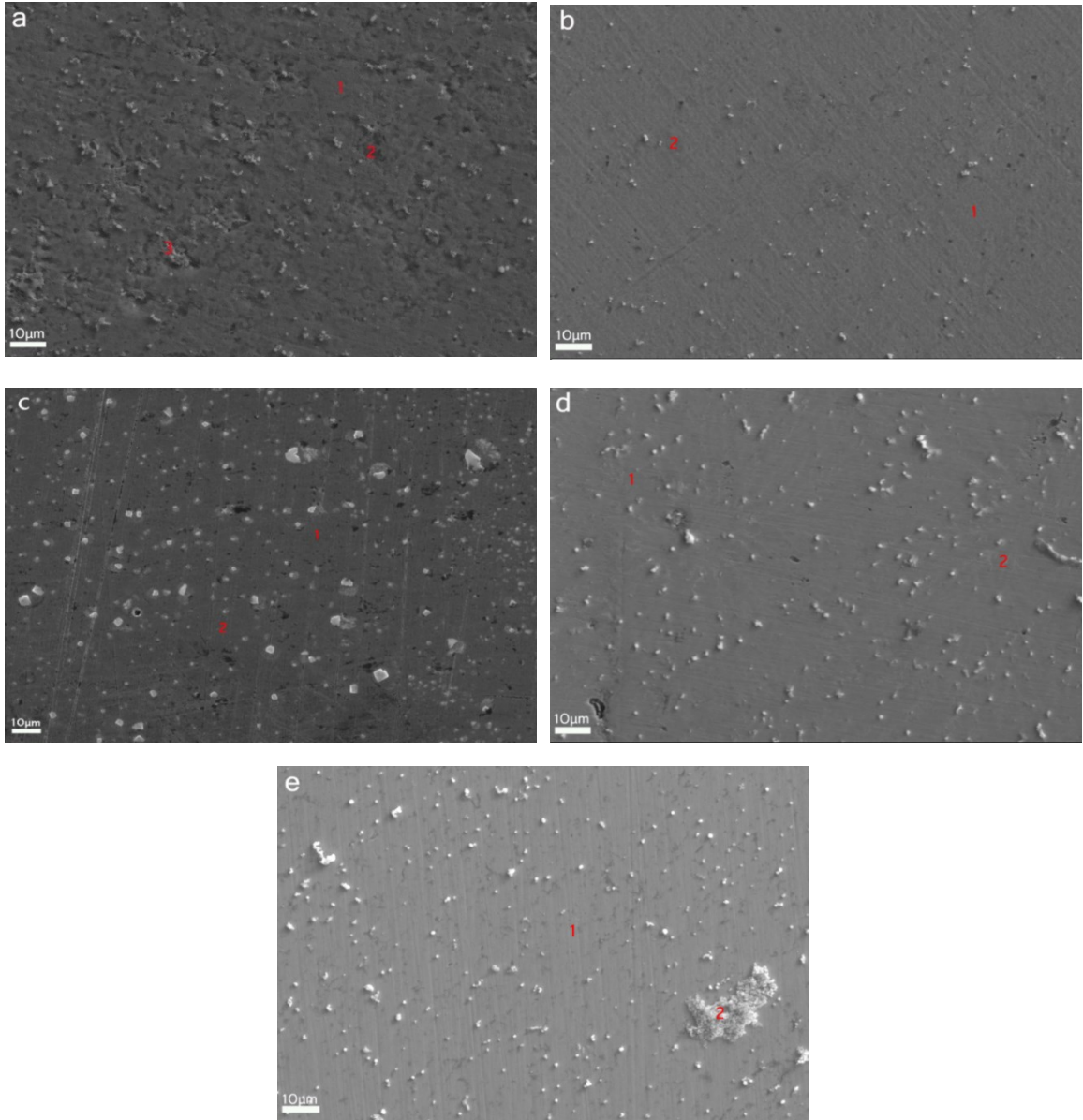


Figure 3.3 SEM images of the surfaces after immersion in NaCl. (a) Cu, (b) 80Cu-20Ni, (c) 50Cu-50Ni, (d) 20Cu-80Ni and (e) Ni.

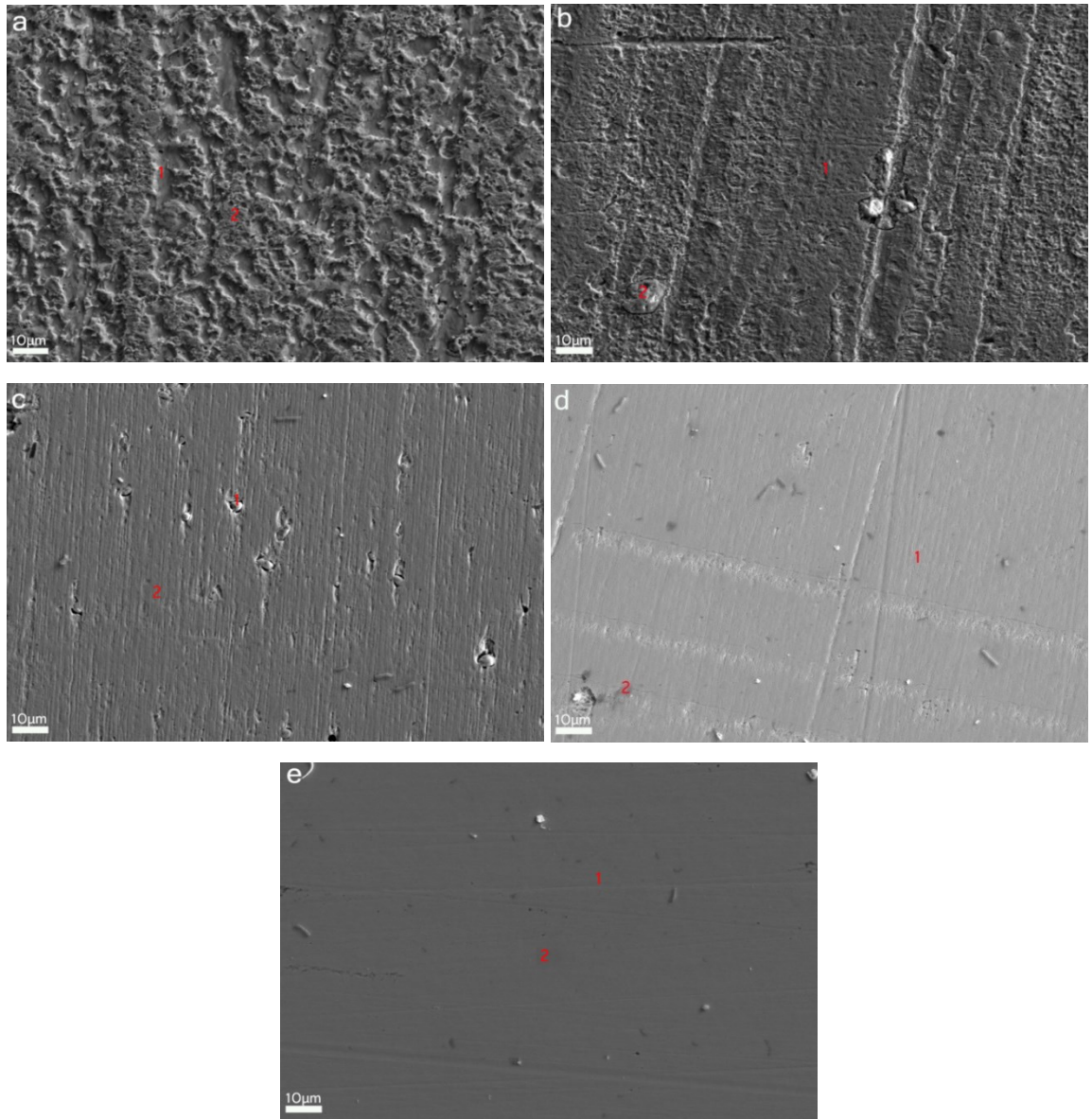


Figure 3.4 SEM images of the surfaces after immersion in HCl. (a) Cu, (b) 80Cu-20Ni, (c) 50Cu-50Ni, (d) 20Cu-80Ni and (e) Ni.

Surface compositions of the samples after the immersion tests were analyzed and are presented in Table 3.1. As shown, after immersion in the NaCl solution, all samples have considerably higher contents of oxygen on surface, implying that oxide

scales formed on the samples. However, the content of oxygen on surfaces of the samples after immersed in the acidic solution is generally very low (except possible oxide inclusion such as spot 1 on sample #3), indicating that no oxide scale formed on the samples during the immersion tests in the acidic solution.

Table 3.1- Spot Energy Dispersive Spectroscopy (EDS) analysis of the samples after immersion in NaCl and in HCl.

Solution selected	Sample NO.		Cu (at.%)	Ni (at.%)	Cl (at.%)	O (at.%)
in NaCl 3 wt.%	#1	Spot 1	75	-	1	24
		Spot 2	75	-	1	24
		Spot 3	81	-	1	18
	#2	Spot 1	75	4	1	20
		Spot 2	72	6	1	21
	#3	Spot 1	40	36	1	23
		Spot 2	38	30	2	30
	#4	Spot 1	15	74	-	13
		Spot 2	16	70	-	14
	#5	Spot 1	-	87	-	13
		Spot 2	-	74	4	22
	in HCl pH=3	#1	Spot 1	99	-	-
spot 2			98	-	-	2
#2		Spot 1	94	6	-	-
		Spot 2	92	8	-	-
#3		Spot 1	6	47	-	47
		Spot 2	50	49	-	1
#4		Spot 1	79	20	-	1
		Spot 2	82	16	-	2
#5		Spot 1	-	98	-	2
		Spot 2	-	98	-	2

The surface composition analysis with EDS confirms the formation of oxides after immersion in NaCl solution. Although the measurement of oxygen content with EDS may not be very accurate, the significant increase in oxygen content is a clear indication of oxidation during the immersion process in the NaCl solution. When

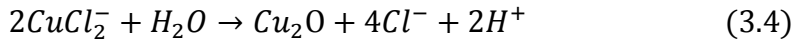
immersed in chloride-containing solutions, the following adsorption process may occur on Cu surface [75]:



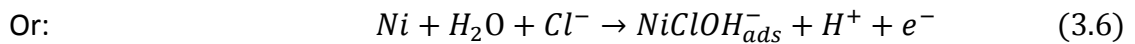
The $CuCl_{ads}^{-}$ precipitates on the surface, forming a porous $CuCl$ film [76]. The dissolution of this adsorbed layer, or the dissolution of copper itself, can produce soluble $CuCl_2^{-}$ [77]:



It is suggested that the presence of high concentration of $CuCl_2^{-}$ at the metal surface causes a hydrolysis reaction, leading to the formation of Cu_2O scale [78, 79]:



This explains the high surface oxygen content detected on the Cu, 80Cu-20Ni and 50Cu-50Ni samples. This corrosion product more or less protects the samples from continuous attack by the chloride ions [80]. For samples of Ni and those contain little Cu, no Cu_2O scale can form. Instead, sparse adsorbed species might form associated with the following possible reactions [81, 82]:



In HCl solution, however, according to Le Chatelier's principle [83], reaction (3.4) and (3.6) may hardly occur due to the presence of high concentration of H^+ . Thus, the samples surfaces were relatively clean with low oxygen contents after immersion in the hydrochloric acid.

Cu is nobler than H_2 in the electromotive series ($E^M = +0.34V$ for the electrode reaction: $Cu^{2+} + 2e^- = Cu$ while Ni has its $E^M = -0.25V$ negative to that of H_2). Thus, one may expect that Cu is resistant to acidic corrosion while Ni is not. However, the situation is different. The hydrolysis product, Cu_2O , can be easily dissolved by the hydrochloric acid [84], thus destroying the barrier to reactions (3.1) - (3.4) according to Le Chatelier's principle, resulting in faster corrosion of copper in the HCl solution. This may explain the rougher surface of Cu-rich samples shown in Figs.3.2 and 3.4 as well as the low oxygen content on surface determined by the EDS analysis (see Table 3.1). The morphologies of the samples with high concentration of Ni are similar after immersion in both NaCl and in HCl. In hydrochloric acid, the oxygen content was even lower than that in NaCl. This is attributed to dissolution of Ni and adsorbed species that are described in Eqs. (3.5) and (3.6).

In order to directly compare the nobilities of Cu and Ni, pure Cu and Ni samples were connected, through a voltmeter, and immersed in the NaCl (3%) and HCl (pH=3.0) solutions, respectively. Results of the measurements showed that in the NaCl solution, Cu had its potential +0.7 mV higher than that of Ni, which means Cu has a less corrosion susceptibility than Ni when immersed in this solution. While in

HCl solution, however, the direction of potential difference is reversed; Cu had its potential -0.6 mV lower than that of Ni, indicating that Cu behaved poorly, compared to Ni, in the hydrochloric acid. This is in agreement with the morphology and composition analysis.

In order to confirm this difference between Cu and Ni in corrosion resistance, weight losses and corresponding volume losses, are shown in table 3.2. In NaCl solution, the two metals underwent similar and almost negligible weight losses. This may be attributed to the fact that NaCl itself is not a strong corrosive solution to Cu and Ni, and that some corrosion weight loss can be compensated by the weight gain from formed corrosion products. In the HCl solution, significant difference can be observed between these two metals. Ni clearly showed higher corrosion resistance than Cu.

When the two metals were connected and immersed in the solutions, in the NaCl solution Cu acted as the cathode and Ni as the anode, while in the acidic solution their roles were switched. In the NaCl solution, corrosion or dissolution of Cu was blocked by its oxide scale, which made Cu appeared to be cathodic. However, based on electron work functions of Cu and Ni, the latter is intrinsically nobler than the former. Thus, intrinsic resistance to corrosion is reflected by the electron behavior while the electrode potential is environment-dependent. The relationship between the electrochemical potential (E^M) and the electron work function (φ^m) of the metal can be generally expressed as the following equation [85]:

$$E^M = \varphi^m + \Delta_s^m \psi \quad (3.7)$$

where the second term on the right side of the equation, $\Delta_s^m \psi$, is the contact potential difference at the metal/solution interface.

Table 3.2- Weight losses of Cu and Ni when respectively immersed in NaCl and HCl solutions in two arrangements: separated and connected.

		$M_i(\text{g})$	$M_f(\text{g})$	$\Delta m(\text{mg})$	$\Delta V(\text{mm}^3)$
Connected in acid	Cu	7.2697	7.2655	-4.2	-0.469
	Ni	8.8865	8.8865	0	0
Separated in acid	Cu	7.2597	7.2566	-3.1	-0.346
	Ni	8.8610	8.8603	-0.7	-0.078
Connected in NaCl solution	Cu	7.7200	7.1998	+0.1	+0.011
	Ni	8.8329	8.8330	-0.2	-0.022
Separated in NaCl solution	Cu	7.1452	7.1451	-0.1	-0.011
	Ni	8.8299	8.8298	-0.1	-0.011

3.3.2 Corrosive wear

The oxide scale plays an important role to protect material from corrosion and may also resist a destructive process combining corrosion and mechanical attacks such as corrosive wear. The wear behaviors of the alloys in the NaCl and HCl solutions were evaluated using a pin-on-disk apparatus. Results of the tests are presented in figure 3.5. As shown, in the NaCl solution, Cu performed better than Ni and the wear loss increased as %Ni was increased. Cu is softer than Ni [51] and is expected to have a lower resistance to wear. Thus, the better performance of Cu in the NaCl solution should be benefit from its oxide scale, which more or less withstood the contact force, protected the surface from further corrosion and wear, minimizing the corrosion-wear synergy. However, in the HCl solution in which no oxide scale formed, the performance of Ni was superior to that of Cu as expected, due to its higher corrosion resistance and hardness.

Figure 3.6 shows SEM images of worn surfaces of three selected samples tested in NaCl solution. It is clear that there existed some scales covering the wear tracks of pure Cu (fig.3.6.a). EDS analysis (see Table 3.3) confirms the existence of high oxygen content. The oxide scales on Cu-rich samples, which adhere to the matrix material, may act as a shield to protect alloys from further wear. While in HCl solution, no sustainable oxides formed (see Figure 3.6 and Table 3.3). In this case, the harder and nobler Ni showed higher resistance to corrosive wear.

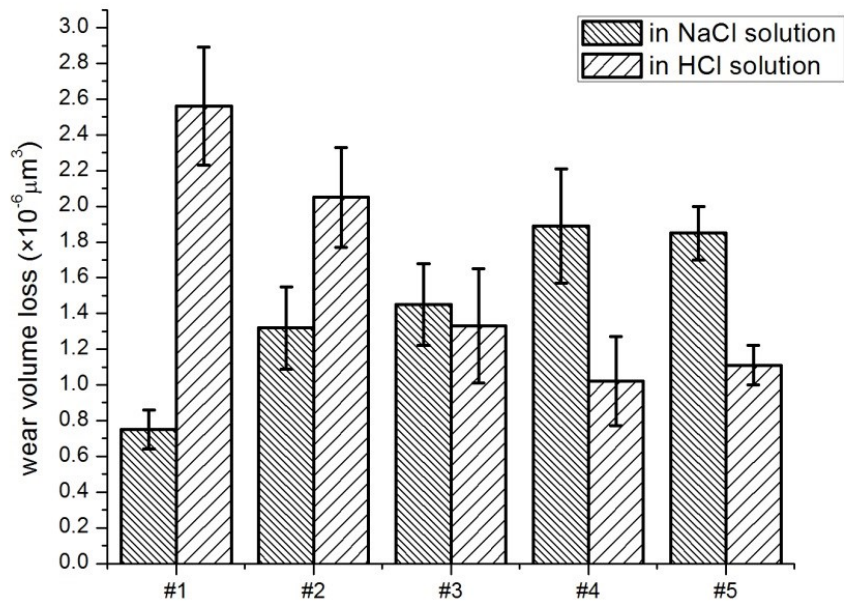
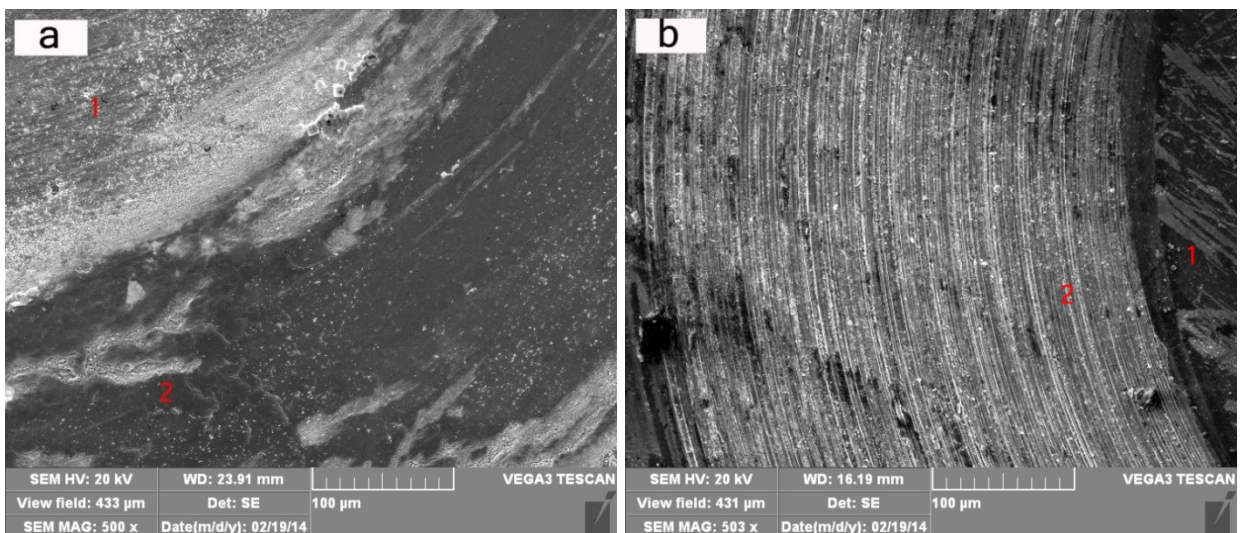


Figure 3.5 Corrosive wear loss of the alloys in two solutions: (1) 3 wt.% NaCl and (2) HCl with a pH=3



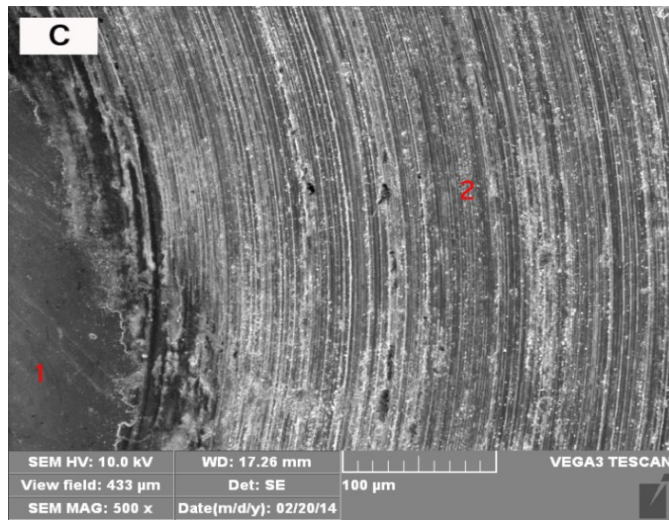


Figure 3.6 SEM images of worn surfaces in NaCl solution of three selected samples: (a) Cu sample (#1), (b) Ni (#5), and (c) 50Cu-50Ni (#3).

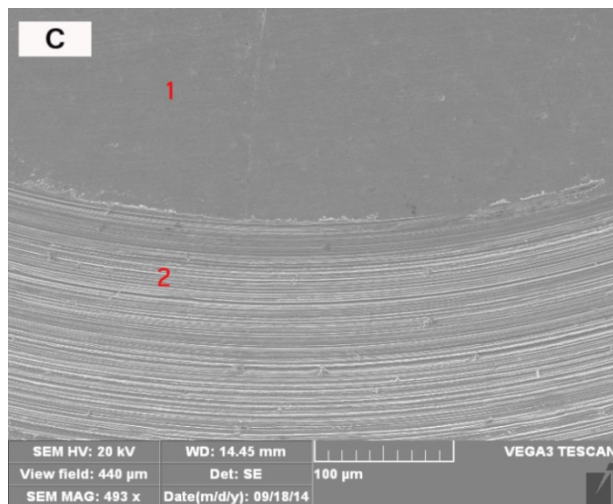
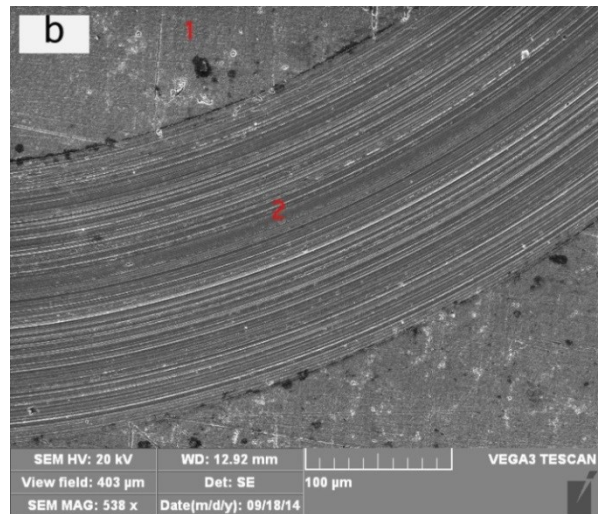
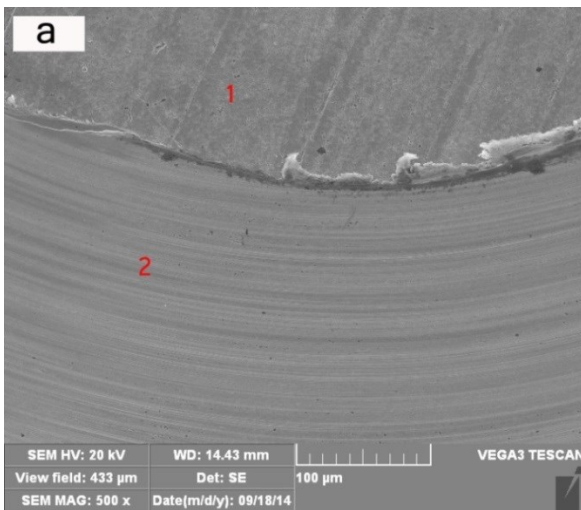


Figure 3.7 SEM images of worn surfaces in HCl of three selected alloys. (a) Cu, (b) Ni, and (c) 50Cu-50Ni.

Table 3.3- Spot Energy Dispersive Spectroscopy (EDS) analysis of the samples after corrosive wear in NaCl and in HCl.

Corrosive medium	Sample NO.		Cu (at.%)	Ni (at.%)	O (at.%)	Cl (at.%)
NaCl (3 wt.%)	#1	Spot 1	81	-	18	1
		Spot 2	62	-	36	2
	#3	Spot 1	58	33	9	-
		Spot 2	42	39	19	-
	#5	Spot 1	-	82	17	-
		Spot 2	-	77	22	1
HCl (pH=3.0)	#1	Spot 1	98	-	2	-
		Spot 2	95	-	5	-
	#3	Spot 1	41	57	2	-
		Spot 2	57	40	3	-
	#5	Spot 1	-	98	2	-
		Spot 2	-	95	5	-

However, if the materials under wear attacks at high speeds at which the oxide scale cannot form timely, the situation would be different. In this study, we also performed high-speed slurry-jet erosion tests using sand-containing NaCl slurry. It should be mentioned that though full removal of oxide scale could not be guaranteed in the present test, no an integrated oxide scale would stay on surface and play a protective role in the erosion process when the surface was eroded by a high-speed slurry flow.

Mass losses of the samples were measured and then converted into volume losses using eq.(2.6). Figure 3.8 illustrates volume losses of the samples during the slurry-jet erosion tests at an impingement angle of 45° and slurry speed of 30 m/s. As shown, the material loss decreased as %Ni increased, different from that observed during the sliding wear tests in the NaCl solution. The increase in the resistance to

slurry-jet erosion is mainly attributed to the fact that there were no protective oxide scales on Cu-rich samples, thus harder Ni-rich samples performed better. Besides, the mechanical strength is related to the work function. A higher EWF corresponds to a larger barrier to the attempt to change the electron state, which will benefit the material's resistance to both corrosion and wear processes.

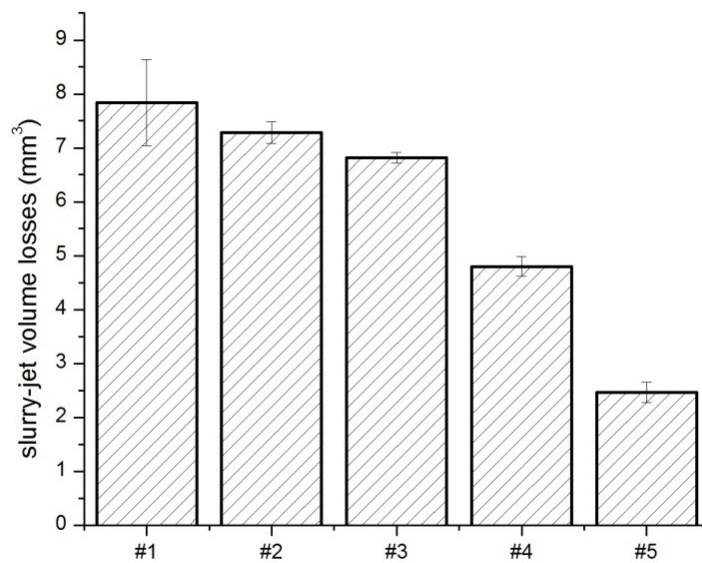


Figure 3.8 Material loss caused by slurry-jet erosion. Slurry: sand-containing NaCl solution.

Eroded surfaces of the alloys were examined under SEM. Figure 3.9 illustrates eroded surfaces of samples Cu, Ni and 50Cu-50Ni. Results of corresponding local composition analysis are given in Table 3.4, which indicates much less oxidation, compared to the case of sliding wear tests.

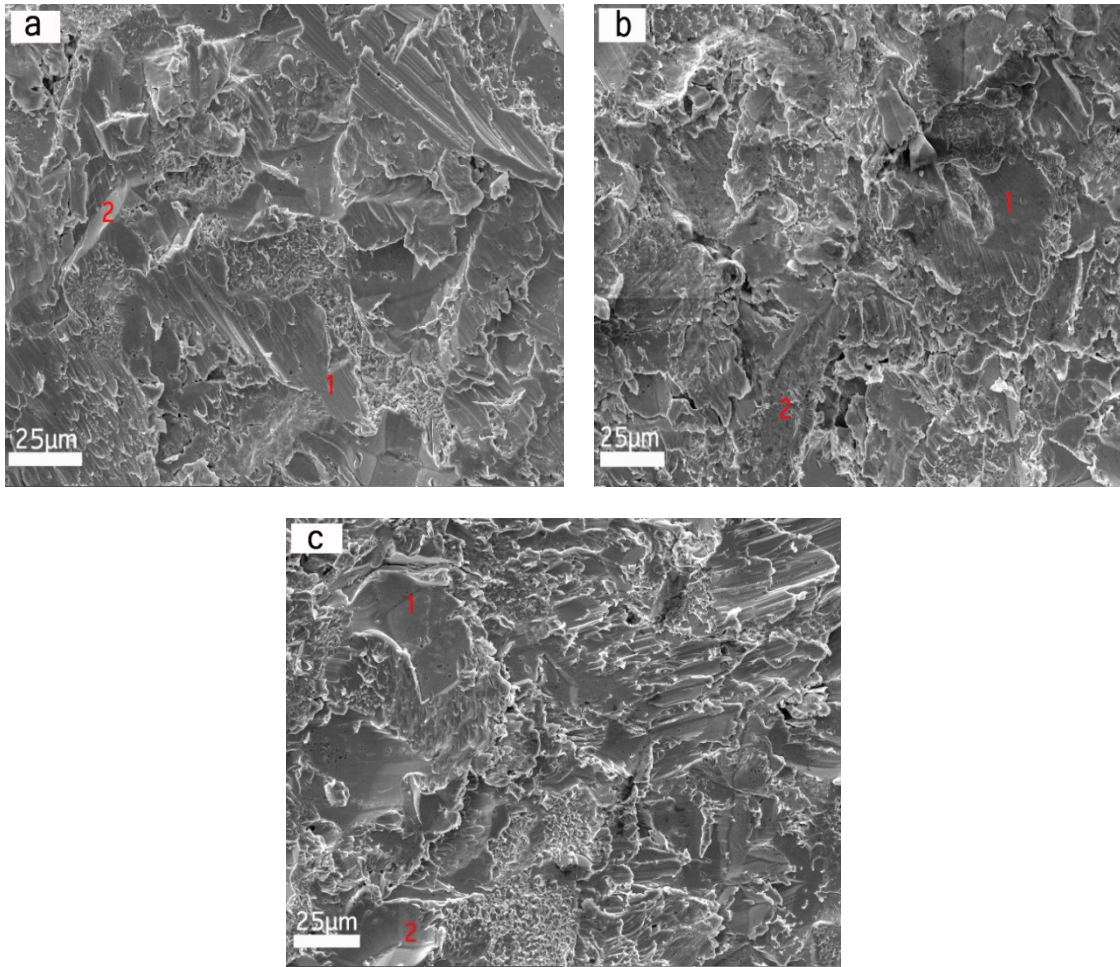


Figure 3.9 Eroded surfaces of (a) Cu, (b) Ni and (c) 50Cu-50Ni.

Table 3.4- EDS analysis of eroded surfaces of three samples.

Sample NO.		Cu (at.%)	Ni (at.%)	O (at.%)	Cl (at.%)
#1	Spot 1	95	-	5	-
	Spot 2	97	-	3	-
#3	Spot 1	56	37	7	-
	Spot 2	50	42	8	-
#5	Spot 1	-	96	4	-
	Spot 2	-	96	3	1

3.4 Summary

The correlation between electron work function of Cu-Ni alloy and its corrosion behaviors in NaCl and HCl solutions, respectively, were investigated. This chapter demonstrated that EWF of Cu-Ni alloy increased with increasing the Ni concentration. In the acidic solution, the alloy dissolved without formation of an oxide scale. In this case, Ni-rich alloys showed higher resistance to corrosion. However, in the NaCl solution, Cu-rich samples exhibited higher resistances to corrosion, mainly due to the formation of oxide scale that more or less protected the samples from further corrosion. The oxide scale also helped reduce wear of Cu-rich samples in the NaCl solution. However, when subject to slurry-jet erosion, Ni-rich samples performed better than Cu-rich ones, since in this case, no oxide scale could form timely. Thus, the harder Ni-rich samples with higher EWF demonstrated higher resistance to erosion caused by the sand-containing NaCl slurry jet. In the HCl solution in which no oxide scale could form, Ni-rich samples performed better than Cu-rich samples during the pin-on-disc tests.

This chapter also demonstrates that the intrinsic nobility of a metal is ultimately governed by its electron stability, reflected by the electron work function. While the electrode potential or electrochemical series is environment-dependent, which is useful as an indicator of likely reactions leading to corrosion, however.

Chapter 4

Dependence Of Metallic Material's Wear

Resistance On Temperature Via The Electron

Work Function

4.1 Objectives

The objectives of this part of study are 1) to illustrate the dependence of the electron work function on the temperature, and 2) to correlate material's wear resistance and the temperature via EWF.

4.2 Experimental procedures

Cu, Ni and carbon steel (CS: 0.25%C, pearlitic steel) samples with dimensions of 20×10×5 mm were polished with 800 and then 1200 grit grinding papers, cleaned with distilled water and acetone. A home-made air-jet erosion tester was used to perform solid-particle erosion tests at elevated temperatures for the sample materials. The impingement angle was set at 90°. AFS 50-70 sand was used for the tests. A mixture of sand and pressed air was delivered through a nozzle of 4 mm in inner diameter and the distance between the nozzle and samples was 20 mm. Three sand particle velocities of 55 m/s (air pressure: 40 psi), 35 m/s (air pressure: 30 psi) and 23 m/s (air pressure: 10 psi) were used for the erosion tests, respectively. The weight loss of samples caused by erosion was determined using a balance with an accuracy of 0.1 mg. Eroded surfaces were examined using a Vega-3 TESCAN Scanning Electron Microscope at 20 kV.

4.3 Results and discussion

Via combination of the correlation between wear and EWF as well as the relation between work function and temperature, i.e. equation (2.12) and equation

(1.28), respectively, the erosion volume loss is expressed as a function of temperature via the effect of temperature on work function:

$$V = K_E \frac{mv^2}{H} = K_{E\varphi} \frac{mv^2(1 - \mu^2)}{\varphi^6} = K'_{E\varphi} \frac{mv^2(1 - \mu^2)}{\left(\varphi_0 - \gamma \frac{(k_B\tau)^2}{\varphi_0}\right)^6} \quad (4.1)$$

The expression for the erosive mass loss can be realized based on this equation, since the mass, m and the volume, V are related based by the density, d as $m=dV$. The expression for mass loss becomes:

$$\text{Mass loss} = \frac{C}{\left(\varphi_0 - \gamma \frac{(k_B\tau)^2}{\varphi_0}\right)^6} \quad (4.2)$$

where $C = K'_{E\varphi} mv^2(1 - \mu^2)d$. C is a complicated parameter which takes both the material's intrinsic properties, i.e. μ and d , and the experimental conditions, i.e. mv^2 into consideration. To better characterize the material's performance under various experimental conditions, we let

$$\beta = \frac{C}{mv^2} = K'_{E\varphi}(1 - \mu^2)d \quad (4.3)$$

So Eq.(4.1) becomes

$$\text{Mass loss} = \frac{C}{\left(\varphi_0 - \gamma \frac{(k_B\tau)^2}{\varphi_0}\right)^6} = \frac{\beta \cdot mv^2}{\left(\varphi_0 - \gamma \frac{(k_B\tau)^2}{\varphi_0}\right)^6} \quad (4.4)$$

According to Eq. (4.2), we have

$$\left(\frac{1}{\text{mass loss}}\right)^{1/6} = C^{-1/6} \left(\varphi_0 - \gamma \frac{(k_B\tau)^2}{\varphi_0}\right) \quad (4.5)$$

To obtain the value for γ , we do the following treatments on this equation, let

$$\left(\frac{1}{\text{mass loss}}\right)^{\frac{1}{6}} = y, \tau^2 = x, \beta^{-\frac{1}{6}} \cdot \varphi_0 = a, \text{ and } C^{-1/6} \cdot \gamma \frac{k_B^2}{\varphi_0} = b, \text{ then we can simplify}$$

Eq.(4.5) as the following:

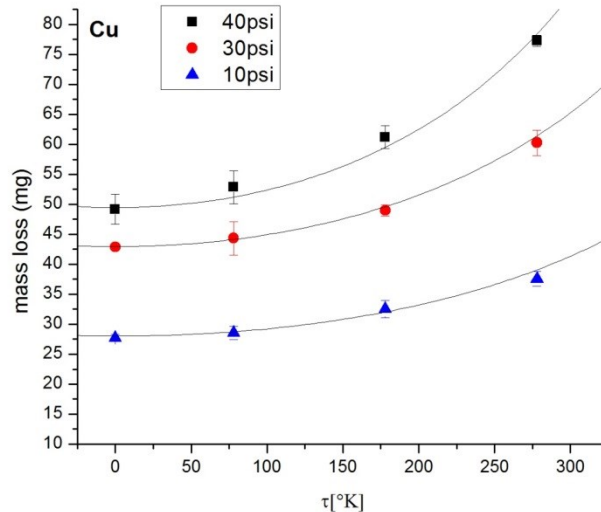
$$y = a - bx \quad (4.6)$$

Linear fitting analysis of this relationship between x and y gives values for both the coefficient a and b . Finally we obtain the value for γ and β through

$$\gamma = \frac{b}{a} \cdot \frac{\varphi_0^2}{k_B^2} \quad (4.7)$$

$$\beta = \frac{C}{mv^2} = \frac{\left(\frac{a}{\varphi_0}\right)^{-6}}{mv^2} \quad (4.8)$$

where $\varphi_0 = \varphi_{295K}$ and this is a parameter that can be measured in experiments and we assume that $\varphi_{steel} \approx \varphi_{Fe}$. The term mv^2 is the kinetic energy of the ejected sand in each test. Figure 5.1 illustrates the mass losses of the samples with respect to temperature at three different sand particle velocities.



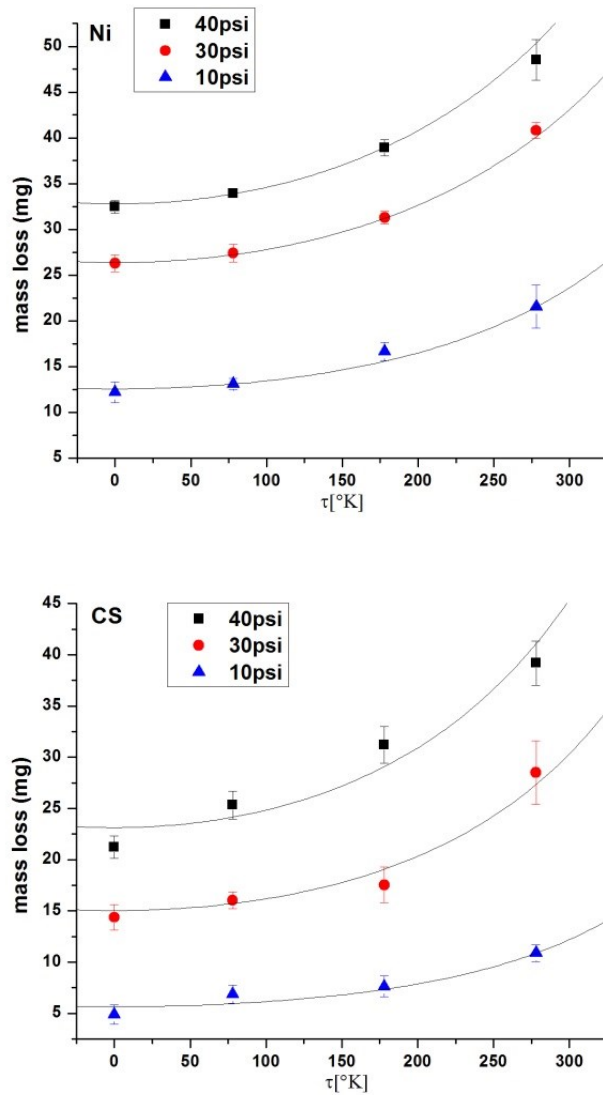


Figure 4.1 Variations in mass loss of copper, nickel and steel samples with temperature and sand particle velocity. The curves present the theoretical prediction and the data points are from the experimental measurements.

Through data fitting, values of γ and β in eq.(8) were determined for the sample materials and are given in Table 4.1. Electron work functions of the materials, $\varphi_0 = \varphi_{295K}$, are $\varphi_0(Cu) = 4.6eV$, $\varphi_0(Ni) = 5.1eV$, $\varphi_0(CS) = 4.6eV$. Since cementite

is an insulative material with low conductivity, the work function of the steel and its variation with temperature should be dominated by those of iron. As shown in Table 4.1, the coefficient γ obtained by data fitting for each sample show minor variations at different particle velocities, implying that γ is a material constant. The coefficient β for each material varied with the velocity of sand particles. As shown, β value increases with decreasing the particle velocity. This could be related to mechanical response of materials to dynamic stresses, which may involve effects of strain rate on stain hardening and failure, influencing the coefficient K_E in eq.(4.1).

Table 4.1- Values of the coefficient γ and β of the materials under different conditions

Particle velocity (m/s)	φ_0 (eV)	Coefficient	Cu	Ni	CS
		γ	2784	3189	3216
55	4.6	$\beta(10^{-3} \frac{eV^6}{(\frac{m}{s})^2})$	0.80	0.81	0.25
		γ	2175	3075	3825
35	5.1	$\beta(10^{-3} \frac{eV^6}{(\frac{m}{s})^2})$	1.09	1.23	0.30
		γ	2026	3262	3633
23	4.6	$\beta(10^{-3} \frac{eV^6}{(\frac{m}{s})^2})$	1.81	1.77	0.36

It should be mentioned that converting the mass losses to volume loss, using $ML = VL \cdot \rho$ and $\rho_{Cu} = 8.96 \text{ g/cm}^3$, $\rho_{Ni} = 8.91 \text{ g/cm}^3$ and $\rho_{CS} \approx 7.85 \text{ g/cm}^3$, one may rank the performance of the materials and see that the volume loss of the carbon steel is smaller than those of Cu and Ni, although its work function is lower than that of Ni and similar to that of Cu. The higher resistance of the carbon steel to erosion is attributed to the strengthening effect of cementite (Fe_3C) in the iron matrix. Such effect should be reflected by the value of β . This study shows that the overall work function of a two-phase material does not well reflect its overall performance, which is determined by both the properties of individual microstructural constituents and their spacial arrangement i.e. the microstructure. However, eq.(4.2) works when the work function is dominated by a conductive microstructure constituent, e.g., iron, and the microstructure does not change much as temperature varies.

Figure 4.2 illustrates corresponding eroded morphologies (SEM) at different temperatures. No obvious oxidation is observed. Under the current erosion condition, no oxide scale could stay on sample surface. Thus, the oxidation effect on erosion was minimized.

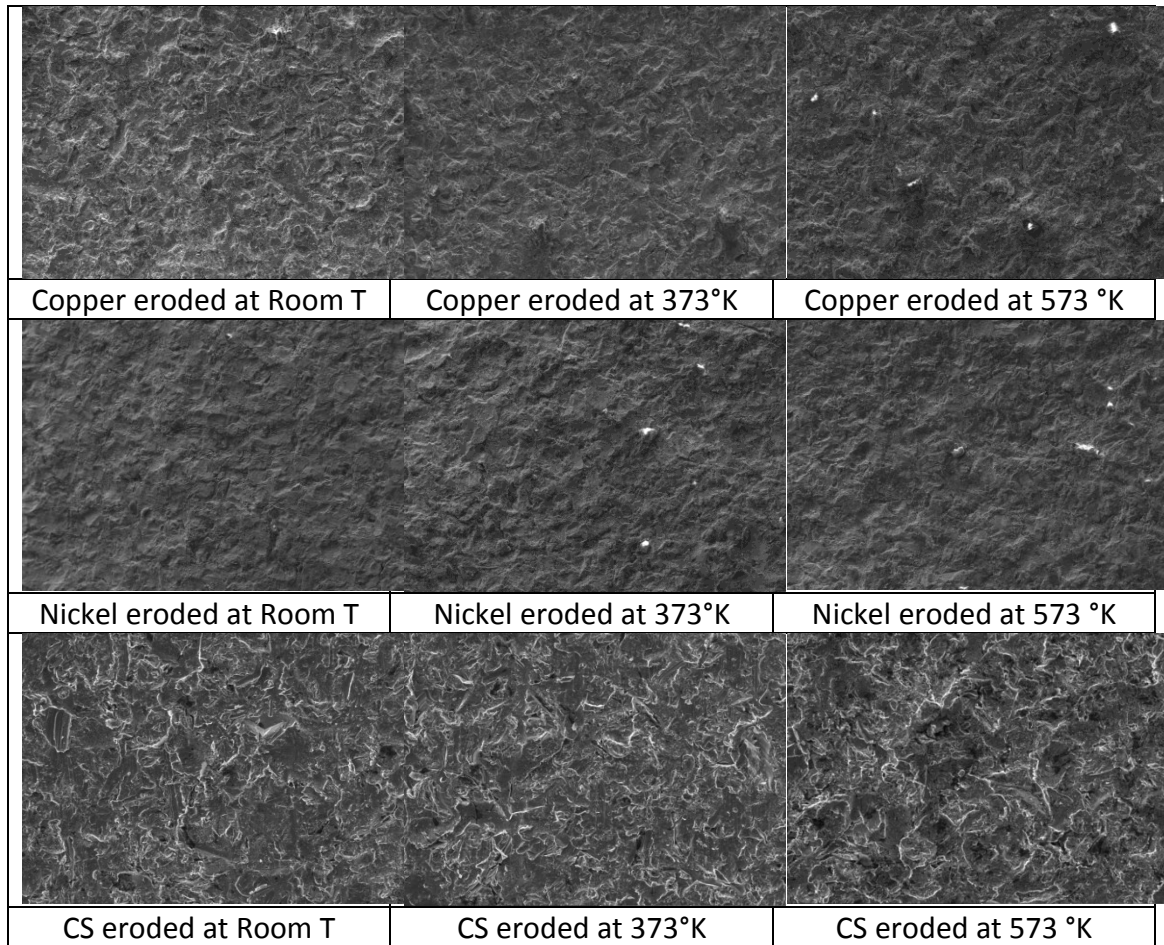


Figure 4.2 SEM images of the eroded surfaces of copper, nickel and carbon steel under room temperature, 100°C and 300°C, respectively.

4.2 Summary

Mechanical properties of metallic materials are intrinsically determined by their electron behavior, which is largely reflected by the electron work function. In this study, temperature-dependent solid-particle erosion model was proposed based on the correlation between hardness and electron work function and the dependence of work function on temperature. Wear losses of copper, nickel and carbon steel as sample materials were measured at different temperatures; results of the tests are in

agreement with the theoretical prediction. This work demonstrates a feasible electronic base for looking into fundamental aspects of wear phenomena, which would also help develop alternative methodologies for tribo-material design and development.

Chapter 5

General Conclusions and Future Work

5.1 General conclusions of the research

In this work, the relationships among EWF, wear resistance and corrosion resistance of the isomorphous Cu-Ni alloys are investigated. Besides, via the dependence of EWF on temperature, the dependence of material's wear resistance on temperature is also discussed.

Chapter 1 provides a general introduction of the electron work function and its correlation to material's properties. It is demonstrated that the EWF is an intrinsic parameter which can characterize the stability of material on an electronic level, thus providing a theoretical basis for correlating EWF and wear and corrosion performances of the materials. As an example which eliminates the influence of second phases, Cu-Ni binary system is introduced and selected as the samples under tests.

In chapter 2, EWFs of the Cu-Ni alloys were measured. It is shown that the overall EWF increases as the Ni concentration increases. Two types of Cu-Ni alloy's wear performances were investigated. It is shown that in air-particle erosion tests, higher EWF corresponds to higher wear resistance. While in sliding wear a reversed trend was observed, which can be attributed to the formation of oxides.

In chapter 2, corrosion and corrosive wear resistance of Cu-Ni alloys in NaCl and HCl solutions are analyzed, respectively. It is demonstrated that samples with higher EWFs performances better in acidic environment, while in sodium chloride

solution, the formed oxide scales reversed the trend. This indicates a non-negligible role that oxide scale plays in corrosion and corrosion involving mechanical attacks such as corrosive wear.

In chapter 4, the influence of temperature and test condition on metallic material's wear resistance was investigated via the high-temperature solid-particle erosion tests. Increase of temperature can decrease EWF and the wear resistance as a result. The wear rates under various sand velocities illustrate that the external experiment parameters can influence the wear rate, while the correlation between EWF and temperature remains independent on environment.

This study shows that EWF is very promising for tribo-materials design and evaluating the intrinsic nobility of metals on a feasible fundamental base.

5.2 Future work

5.2.1 Influence of second phases on the mechanical/corrosion properties-EWF correlation

In the present study, we use the isomorphous Cu-Ni alloys as sample materials to prevent the influence of second phases. In realistic industrial applications, however, materials with various second phases will be used, such as carbon steel and cast irons. Future work would include studies of the influence of the second phases, for instance, the interaction between inclusions and the matrix.

5.2.2 More fundamental studies on the relationship between EWF and the electrode potential

A general relationship between EWF and the electrode potential is demonstrated in chapter 1. There are also many references discussing the relationship between EWF and electrode potential. However, none of them has ever illustrates this relationship on an electronic scale, since the influence of the solution (environment) can be very complicated. In the future work, efforts would be made to build a bridge between the electrode potential and the intrinsic parameter-EWF.

5.2.3 Using improved models and experiment techniques

In both chapter 2 and 3, we operated solid-particle erosion tests to eliminate the possible influence of oxidation. However, under high-speed sand flow, there is more or less some plastic deformation occurs besides the plastic deformation on the surface. This will influence the correlation that between EWF and wear rate to a certain extent. Similarly, in chapter 4, different sand velocities may correspond to different wear mechanisms, thus making the judgment of the independence of $\varphi - T$ on environment difficult. Besides, even much less than that in sliding wear tests, our surface content tests did show some oxidation during the erosion process. Thus, a more complicate wear mode which is closer to the real erosion test, as well as a vacuum or an inert gas experiment environment would improve the theoretical prediction and the accuracy of the experiment data.

Reference

1. S. Halas, 100 years of work function, *Materials Science-Poland* 24 (2006) 951-967.
2. T.C. Leung, C.L. Kao, W.S. Su, et al., Relationship between surface dipole, work function and charge transfer: Some exceptions to an established rule, *Physical Review B* 68 (2003) 195408.
3. Oh, J.K., et al., The development of microgels/nanogels for drug delivery applications, *Progress in Polymer Science*, 2008. **33**(4) 448-477.
4. W. Li, D. Li, Influence of surface morphology on corrosion and electronic behavior, *Acta Materialia*, 2005.
5. L. Zha, B. Banik, and F. Alexis, Stimulus responsive nanogels for drug delivery, *Soft Matter*, 2011. **7**(13) 5908-5916.
6. B. Bhushan, A.V. Goldade, Measurements and analysis of surface potential change during wear of single-crystal silicon (100) at ultralow loads using Kelvin probe microscopy, *Applied Surface Science* 157 (2000) 373-381.
7. D. Kabra, et al., High Efficiency Composite Metal Oxide-Polymer Electroluminescent Devices: A Morphological and Material Based Investigation, *Advanced Materials*, 2008. **20**(18) 3447-3452.
8. J.-H. Ryu, et al., Self-cross-linked polymer nanogels: a versatile nanoscopic drug delivery platform, *Journal of the American Chemical Society*, 2010. **132**(48) 17227-17235.
9. R. Grover, et al., Kelvin probe force microscopy as a tool for characterizing chemical sensors, *Applied Physics Letters*, 2004. **85**(17) 3926.
10. H.R. Moutinho, et al., Scanning Kelvin Probe Microscopy of CdTe Solar Cells Measured under different Bias Conditions, *MRS Proceedings*, 2009. 1165.(M08-28).
11. W. Li, D. Li, Effects of elastic and plastic deformations on the electron work function of metals during bending tests, *Philosophical Magazine*, 2004. **84**(35) 3717-3727.
12. D. Li, L. Wang, and W. Li, Effects of grain size from micro scale to nanoscales on the yield strain of brass under compressive and tensile stresses using a Kelvin probing technique, *Materials Science and Engineering: A*, 2004. **384**(1-2) 355-360.
13. http://en.wikipedia.org/wiki/Ultraviolet_photoelectron_spectroscopy.
14. A. Zharin, D.A. Rigney, Application of a constant potential difference technique for on-line rubbing surface monitoring (review), *Tribol. Lett.* 4 (1998) 205-213
15. I.D. Baikie, et al., Multitip scanning bio-Kelvin probe, *Review of Scientific Instruments*, 1999. **70**(3) 1842.
16. N.A. Surplice, R.J. Darcy, A critique of Kelvin Method of Measuring Work Functions, *Journal of Physics E-Scientific Instruments* 3 (1970) 477-482.

17. A. Schaak, R. Imbihl, Spiral waves and formation of low work function areas in catalytic NO reduction with hydrogen on a Rh(111) surface, *The Journal of Chemical Physics*, 2002. **116**(20) 9021.
18. W. Li, D. Li, Effect of surface geometrical configurations induced by microcracks on the electron work function. *Acta Materialia*, 2005. **53**(14) 3871-3878.
19. Anatoly L. Zharin, David A. Rigney, application of the contact potential difference technique for on-line rubbing surface monitoring (review), *Tribology Letters*, 1998. 4(2) 205-213.
20. H.B. Michaelson, Work functions of the elements, *J. Appl. Phys.* 21 (1950) 536-540.
21. H.L. Skriver, N.M. Rosengaard, Surface-Energy and Work Function of Element Metals, *Phys. Rev. B* 46 (1992) 7157-7168.
22. H.L. Skriver, N.M. Rosengaard, Abinitio Work Function of Elemental Metals, *Phys. Rev. B* 45 (1992) 9410-9412.
23. T. Durakiewicz, et al., Electronic work-function calculations of polycrystalline metal surfaces revisited, *Physical Review B*, 2001. **64**(4).
24. S.Halas, et al., Work functions of elements expressed in terms of the Fermi energy and the density of free electrons, *Journal of Physics-Condensed Matter* 10 (1998) 10815-10826.
25. W. Li, D.Y. Li, Effects of dislocation on electron work function of metal surface, *Materials Science and Technology*, 2002. **18**(9) 1057-1060.
26. R.H. Baughman, J.M. Shacklette, A.A. Zakhidov, S. Stafstrom, Negative poisson's ratios as a common feature of cubic metals, *Nature* 392 (1998) 362-365.
27. A.R. Miedema, Electronegativity Parameter for Transition-metals-Heat of Formation and Charge Transfer in Alloys, *Journal of the Less-Common Metals* 32 (1973) 117-136.
28. A.R. Miedema, Surface Energies of Solid Metals, *Z. Metallk.* 69 (1978) 287-292.
29. A.R. Miedema, R. Boom, F.R. Deboer, Heat of Formation of Solid Alloys, *Journal of the Less-Common Metals* 41 (1975) 283-298.
30. A.R. Miedema, F.R. Deboer, P.F. Dechatel, Empirical Description of the Role of Electronegativity in Alloy Formation, *Journal of Physics F-Metal Physics* 3 (1973) 1558-1576.
31. K.K. Kalazhokov, A.S. Gonov, Z.K. Kalazhokov, On the calculation of the surface energy of a face of a single crystal through the electron work function of this face, *Russian Metallurgy* (1996) 39-41.
32. D. Li, W. Li, Electron work function: A parameter sensitive to the adhesion behavior of crystallographic surfaces, *Applied Physics Letters*, 2001. **79**(26) 4337.
33. W. Li, D. Li, A simple method for determination of the electron work function of different crystallographic faces of copper, *physica status solidi (a)*, 2003. **196**(2) 390-395.

34. C. W. Lung, N. H. March, *Mechanical Properties of Metals: Atomistic and Fractal Continuum Approaches*, World Scientific Pub. Co. Inc.; Singapore 1999.
35. I. Brodie, Uncertainty, topography, and work function, *Physical Review B*, 1995. **51**(19) 13660-13668.
36. G. Hua, D. Li, Generic relation between the electron work function and Young's modulus of metals, *Applied Physics Letters*, 2011. **99**(4) 041907.
37. R. Peierls, The size of a dislocation, *Proceedings of the Physical Society*, 1940. **52**(1) 34-37.
38. F. R. N. Nabarro, Dislocations in a simple cubic lattice, *Proceedings of the Physical Society*, 1947. **59**(2) 256-272.
39. J. P. Hirth and J. Lothe, *Theory of Dislocations*, Wiley, New York 1982.
40. J. F. W. Bishop and R. Hill, XLVI. A theory of the plastic distortion of a polycrystalline aggregate under combined stresses, *Philos. Mag., Ser. 7*, 1951. **42**(327), 414–427.
41. P.H. Rieger, *Electrochemistry*, Chapman & Hall, New York, 1994.
42. C.H. Hamann, A. Hamnett, W. Vielstich, *Electrochemistry*, Wiley-VCH, Weinheim, New York 1998.
43. J.O.M. Bockris, B.E. Conway, E. Yeager, *Comprehensive treatise of electrochemistry*, Vol.1, Plenum Press, New York 1980.
44. J. Schell, P. Heilmann, D.A. Rigney, Friction and wear of Cu-Ni alloys, *Wear*, 1982. **75**(2) 205-220.
45. N. Bhuchar, et al., Detailed study of the reversible addition–fragmentation chain transfer polymerization and co-polymerization of 2-methacryloyloxyethyl phosphorylcholine, *Polymer Chemistry*, 2011. **2**(3) 632-639.
46. J.A. Paces, William R. Opie, *Copper-nickel alloys*, United States (P) 3488188(Jan 6, 1970).
47. J.B. Singh, W. Cai, and P. Bellon, Dry sliding of Cu–15wt%Ni–8wt%Sn bronze: Wear behaviour and microstructures, *Wear*, 2007. **263**(1-6) 830-841.
48. M. Ahmed, R. Narain, The effect of molecular weight, compositions and lectin type on the properties of hyperbranched glycopolymers as non-viral gene delivery systems, *Biomaterials*, 2012. **33**(15) 3990-4001.
49. G. Franks, J. O’Shea, and E. Forbes, Improved solid-liquid separations with temperature responsive flocculants: A review, *Chemeca 2012: Quality of life through chemical engineering: 23-26 September 2012*, Wellington, New Zealand, 2012, 1062.
50. G. Hua, D. Li, The correlation between the electron work function and yield strength of metals, *Physica Status Solidi (b)*, 2012. **249**(8) 1517-1520.
51. H. Lu, G. Hua, and D. Li, Dependence of the mechanical behavior of alloys on their electron work function—An alternative parameter for materials design, *Applied Physics Letters*, 2013. **103**(26) 261902.
52. R. W. Revie, *Corrosion and Corrosion Control*, 4th edition, Wiley, New York, 2008.

53. S. Tao, D. Li, Nanocrystallization effect on the surface electron work function of copper and its corrosion behaviour, *Philosophical Magazine Letters*, 2008. **88**(2) 137-144.
54. A.K. Neufeld, et al., The initiation mechanism of corrosion of zinc by sodium chloride particle deposition, *Corrosion Science*, 2002. 44(3) 555-572.
55. A.A. Nazeer, et al., Effect of glycine on the electrochemical and stress corrosion cracking behavior of Cu10Ni alloy in sulfide polluted salt water, *Industrial & Engineering Chemistry Research*, 2011. 50(14) 8796-8802.
56. W.C. Stewart, F.L. Laque, Corrosion resisting characteristics of iron modified 90:10 cupro nickel alloy, *Corrosion*, 1952. 8(8) 259-277.
57. J.M. Popplewell, R.J. Hart, J.A. Ford, The effect of iron on the corrosion characteristics of 90-10 cupro nickel in quiescent 3-4% NaCl solution. *Corrosion Science*, 1973. 13(4) 299-309.
58. Z.R. Liu, D. Li, The electronic origin of strengthening and ductilizing magnesium by solid solutes, *Acta Materialia*, 2015. **89** 225-233.
59. W. Li, D. Li, Characterization of interfacial bonding using a scanning Kelvin probe, *Journal of Applied Physics*, 2005. **97**(1) 014909.
60. S.W. Watson, et al., Methods of measuring wear-corrosion synergism, *Wear*, 1995. 181-182(part 2) 476-484.
61. Mischler, S., S. Ayrault, and D. Landolt, Investigation of Tribocorrosion of TiC Coatings Using Electrochemical Techniques, *Materials Science Forum*, 1997. **247**, 9-18.
62. D. Landolt, et al., Electrochemical methods in tribocorrosion: a critical appraisal, *Electrochimica Acta*, 2001. 46(24-25) 3913-3929.
63. X.Y. Wang and D.Y. Li, Investigation of the synergism of wear and corrosion using an electrochemical scratch technique, *Tribology Letters*, 2001. 11(2).
64. Wang, X.Y. and D.Y. Li, Application of an electrochemical scratch technique to evaluate contributions of mechanical and electrochemical attacks to corrosive wear of materials, *Wear*, 2005. **259**(7-12) 1490-1496.
65. T.-H. Tsai, Y.-F. Wu, and S.-C. Yen, A study of copper chemical mechanical polishing in urea-hydrogen peroxide slurry by electrochemical impedance spectroscopy, *Applied Surface Science*, 2003. **214**(1-4) 120-135.
66. P. Schmutz, G.S. Frankel, Influence of Dichromate ions on corrosion of pure aluminum and AA2024-T3 in NaCl solution studied by AFM scratching, *Journal of the Electrochemical Society*, 1999. 146(12) 4461-4472.
67. X.X. Jiang, et al., Accelerative effect of wear on corrosion of high-alloy stainless steel, *Corrosion*, 1993. 49(10) 836-841.
68. A. Kiejna, et al., The temperature dependence of metal work functions, *Journal of Physics F: Metal Physics*, 1979. 9(7) 1361-1366.
69. G. Comsa, A. Gelberg, and B. Iosifescu, Temperature Dependence of the Work Function of Metals (Mo,Ni), *Physical Review*, 1961. **122**(4) 1091-1100.
70. R. Rahemi, D. Li, Variation in electron work function with temperature and its effect on the Young's modulus of metals, *Scripta Materialia*, 2015. **99**: 41-44.

71. H. Lu, D. Li, Correlation between the electron work function of metals and their bulk moduli, thermal expansion and heat capacity via the Lennard-Jones potential, *physica status solidi (b)*, 2014. **251**(4) 815-820.
72. J.M. Howe, *Interfaces in Materials: Atomic Structure, Thermodynamics and Kinetics of Solid-Vapor, Solid-Liquid and Solid-Solid Interfaces*, John Wiley & Sons, New York, 1997.
73. I.M.Hutchings, *Tribology-friction and wear of engineering materials*, Edward Arnold, London, 1992.
74. Ernest Rabinowicz, *Friction & Wear of Materials*, 2nd ed., John Wiley & Sons, Inc., 1995.
75. J.P. Diard, et al., Copper electrodisolution in 1 M HCl at low current densities. I. General steady-state study, *Electrochimica Acta*, 1998. 43(16-17) 2469-2483.
76. F.K. Crundwell, The anodic dissolution of 90% Copper-10% Nickel alloy in hydrochloric acid solutions, *Electrochimica Acta*, 1991. 36(14) 2135-2141.
77. G. Kear, et al., Electrochemical corrosion behaviour of 90-10 Cu-Ni alloy in chloride-based electrolytes, *Journal of Applied Electrochemistry*, 2004. 34(7) 659-669.
78. A.L. Bacarella, J.C. Griess Jr, The anodic dissolution of copper in flowing sodium chloride solutions between 25°C and 175°C, *Journal of the Electrochemical Society*, 1973. 120(4) 459-465.
79. C. Deslouis, et al., Electrochemical behaviour of copper in neutral aerated chloride solution. I. Steady-state investigation, *Journal of Applied Electrochemistry*, 1988. 18(3) 374-383.
80. E.M. Sherif, S.-M. Park, Inhibition of copper corrosion in acidic pickling solutions by N-phenyl-1,4-phenylenediamine, *Electrochimica Acta*, 2006. **51**(22) 4665-4673.
81. A. Bengali, K. Nobe, Electrodisolution kinetics of Nickel in concentrated acidic chloride solutions, *J. Electrochem. Soc.*, 1979.126(7) 1118-1123.
82. S.G. Real, et al., Influence of chloride concentration on the active dissolution and passivation of nickel electrodes in acid sulfate solutions, *J. Electrochemical. Soc.*, 137(6) 1696-1702.
83. R.A. Burns, *Fundamentals of chemistry (4th edition)*, Prentice Hall, New Jersey, 2002.
84. D.Nicholls, *Complexes and first-row transition elements*, Macmillan Press, London, 1973.
85. O'.M.B. John, U.M.K. Shahed, *Surface electrochemistry: a molecular level approach*, Springer, New York, 1993.